國 立 交 通 大 學

電子物理系

博 士 論 文

半導體奈米結構電性傳輸
與奈米元件接點電阻之研究

Electrical Transport of Semiconducting Nanostructures

and Impact of Nanocontact on Nanoelectronics

研 究 生：林彥甫

指導教授：簡紋濱 教授

中 華 民 國 九 十 九 年 七 月

半導體奈米結構電性傳輸與奈米元件接點電阻之研究

Electrical Transport of Semiconducting Nanostructures and Impact of Nanocontact on Nanoelectronics
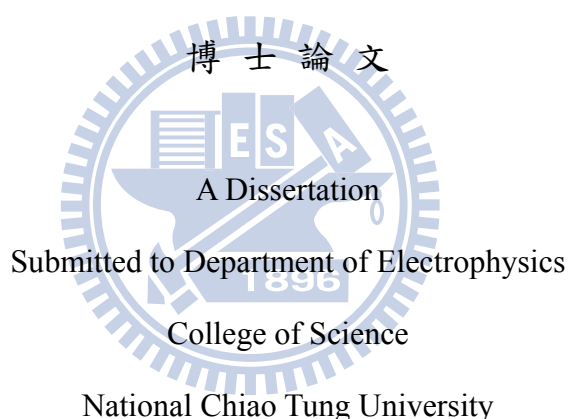
研 究 生：林彥甫 　　　　　　　Student：Yen-Fu Lin

指導教授：簡紋濱 　　　　　　　Advisor：Prof. Wen-Bin Jian

國 立 交 通 大 學

電 子 物 理 系

博 士 論 文

A Dissertation

Submitted to Department of Electrophysics

College of Science

National Chiao Tung University

in partial Fulfillment of the Requirements

for the Degree of

Doctor of Philosophy

in

Electrophysics

July 2010

Hsinchu, Taiwan, Republic of China

中華民國九十九年七月

半導體奈米結構電性傳輸與奈米元件接點電阻之研究

學生: 林彥甫　　　　　　　　　　　指導教授: 簡紋濱 教授

國立交通大學電子物理系博士班

摘要

　　過去數十年間，藉由物理與化學的方法各式各樣半導體奈米線被成功的製造。透過由上而下或由下而上的組裝方法，這些半導體奈米線已被廣泛地應用於研究單電子電晶體、場效電晶體或光電元件等領域中。但在大多數的研究中由於奈米電子元件多具有兩點(Two-probe)的電極結構，因此透過該兩點電極結構，系統性地徹底掌握本質奈米線電性傳輸特性是一項相當重要的研究議題。在過去的文獻中雖然有許多半導體奈米線電性的研究被報導，但對於所量測到的電性傳輸行為究竟是本質奈米線所主導或由於接點電阻所造成的效應並沒有一個深入的探討。本篇論文將透過兩點電極結構深入研究接點電阻在半導體奈米線元件中所扮演的角色，並探求本質氧化鋅(ZnO)、磷化銦(InP)、磷化鎵(GaP)半導體奈米線與聚苯胺(polyaniline)奈米纖維的傳輸特性。
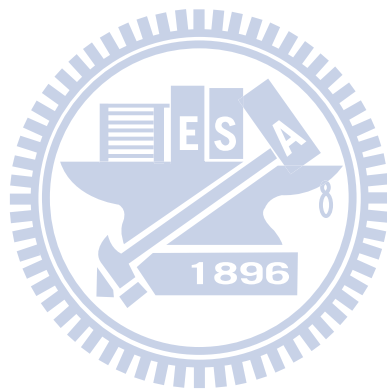
　　本實驗主要分成三大部分，在第一部分的研究裡，我們利用氧化鋅(ZnO)奈米線製造出多組具有兩點電極的奈米線元件，並系統性地研究接點電阻在奈米元件中的影響。我們發現依據與溫度相依的電流-電壓關係曲線圖與電阻的分析，兩點氧化鋅奈米線元件可區分成雙邊歐姆接觸(two Ohmic)、單邊蕭特基接觸(one Schottky)與背對背蕭特基接觸(back-to-back Schottky)等三種類型。

發現由接點電阻所主導的背對背蕭特基奈米電子元件，其溫度與電阻關係曲線圖可藉由 Mott 變程跳躍傳輸模型(variable range hopping) $R \propto \exp((T_0 / T)^{1/p})$ 來加以說明。在接點電阻所主導的樣品中，Mott 變程跳躍傳輸模型的指數函數 p 值，隨著室溫接點電阻率的上升逐漸由 2 上升到 4，意味著變程跳躍傳輸模型在接點系統中，由低維度擴展至高維度的變程跳躍傳輸機制。更進一步地，藉由了解接點電阻在奈米線元件中所扮演的角色，我們可以成功地探究本質氧化鋅(ZnO)、磷化銦(InP)與磷化鎵(GaP)半導體奈米線電性傳輸特性。

由於了解到接點電阻在奈米線元件中所具有的影響。因此，第二部分的研究裡，我們針對磷化銦(InP)奈米線元件進行研究，探求接點電阻與本質奈米線電阻所主導的電子元件在光與氣體的環境中其反應是否具有差異化。實驗過程中，我們採用標準電子束微影的方式製作出多組磷化銦(InP)奈米線電子元件，藉由分析其變溫電阻變化曲線圖，我們可以成功地將樣品區分為奈米線所主導(nanowire-dominated)與接點電阻所主導(contact-dominated)的兩類型元件。在本質奈米線所主導的磷化銦(InP)電子元件中，其高、低溫部分的溫度-電阻關係圖分別可以使用熱活化傳輸理論與三維變程式跳躍傳輸理論來加以說明。更進一步地，將磷化銦奈米線電子元件曝照於光與氧氣的環境下，我們發現無論是奈米線或接點電阻所主導的奈米元件皆具有曝照前/後電阻的變化。令人訝異的是接點電阻所主導的奈米線電子元件無論在曝照光或氣體的反應下皆具有較高的電阻變化率出現。

第三部分的研究中，我們探討有機半導體奈米材料-聚苯胺(polyaniline)奈米纖維的電性傳輸性質。實驗中，藉由介面聚合的化學方法，聚苯胺(polyaniline)奈米纖維成功的被合成。在酸、鹼溶液的摻雜(doping)與去摻雜(dedoping)化學反應中，我們發現聚苯胺奈米纖維之薄膜樣品，其與溫度相依的電阻皆依循著

$\ln R \propto (T)^{-1/2}$ 關係式變化。另一方面，為了探究單根聚苯胺(polyaniline)奈米纖維本質電性傳輸機制，我們首次利用介電泳動法成功地製作出多組具單根纖維之奈米元件。透過系統化的分析與研究，其電性傳輸實驗結果可用 charge-energy-limited-tunneling 理論來加定量說明之。

Electrical Transport of Semiconducting Nanostructures and Impact of Nanoocntact on Nanoelectronics

Student: Yen-Fu Lin   Advisor: Prof. Wen-Bin Jian

Institute of Electrophysics

National Chiao Tung University

Abstract

Various semiconductor nanowires have been synthesized by using either physical or chemical growth methods in the past decades. These nanowires applied to single electron transistors, field-effect transistors, optoelectronics, and nanoelectronics through top-down or bottom-up assembling approaches has been immediately demonstrated. Because of most nanoscale electronics having two-probe configuration as the source and drain electrodes, identification and determination of intrinsic electrical properties of nanowires and the contribution of nanocontact through a systematic procedure of this two-probe approach become very important. Although a lot of two-probe nanoelectronics and applications have been demonstrated in previous reports, the electrical properties bringing either from the nanocontacts or from the nanowires have not been uncovered clear yet. In this work, a two-probe technique was adopted to explore electrical properties of ZnO, InP, GaP nanowires and polyaniline nanofibers.

The first portion of this work is to utilize high quality ZnO nanowires to

fabricate two-probe nanodevices and to survey the impact of nanocontact on nanowire based nanoelectronics. According to temperature behaviors of current-voltage curves and resistances, the devices could be grouped into three types, including two Ohmic contacts, one Ohmic and one Schottky contacts, and two back-to-back Schottky contacts. The nanocontact could be treated as disordered system and be explained by Mott variable range hopping model for electrons of the form $R \propto \exp((T_0/T)^{1/p})$. The exponential parameters of Mott variable range hopping theory rises from 2 to 4 with an increase of specific contact resistivity at room temperature, implying a change from one- to three-dimensional hopping. Moreover, after understanding how to distinguish the nanowire- and contact-dominated nanodevices, we demonstrate that the two-probe measurement can be applied to the exploration of the intrinsic properties of semiconductor nanowires. This two-probe measurement approach also works on highly resistive nanowires without an Ohmic contact issue. By using this method, electron transport behaviors, resistivity, and carrier concentrations of ZnO, InP, and GaP semiconductor nanowires have been investigated.

The interface problems in nanowire-based electronics play important roles due to the reason that the reduced contact area in nanoelectronics multiplies enormously the contribution of electrical contact properties. The second portion is to illustrate the sensitivity difference in response to light and oxygen gas between the nanowire- and contact-dominated InP nanowire devices. By using a standard electron-beam lithography technique, two-probe InP nanowire devices were fabricated. Although the InP were picked up from the same source sample and the dimensions of the nanowires and nanodevices were also kept the same, the room-temperature resistance of these devices varied considerably. It was conjectured the difference of room-temperature comes from the contribution of

contact resistance. According to the temperature behaviors, the nanowire devices can be categorized into nanowire- and contact-dominated ones. The temperature dependent resistances follow the thermally activated and three-dimensional Mott variable range hopping transport at high and low temperatures, respectively. Both nanowire- and contact-dominated devices were exposed to light and oxygen gas to see any difference. In comparison with the nanowire-dominated devices, the contact-dominated InP nanowire devices always exhibit a much higher ratio of resistance changes in response to either light or oxygen gas exposures.

The last portion of this work is to study the electrical transport of polyaniline nanofibers. Polyaniline nanofibers were synthesized by using polymerization at the interface of immiscible solvents. They exhibit a uniform nanoscale morphology rather than agglomeration with granular structures as that produced via conventional chemical oxidation. The as-synthesized polyaniline nanofibers are doped (dedoped) with an HCl acid (NH_3 base) and their temperature behaviors of resistances all follow an exponential function with an exponent of $T^{-1/2}$. To achieve the measurement of conduction mechanism in a single nanofiber, the dielectrophoresis technique is implemented to position nanofibers on top of and across two Ti/Au electrodes patterned by electron-beam with a nanogap of 100-200 nm. Their temperature behaviors and electric field dependences are unveiled and the experimental results agree well with the theoretical model of charge-energy-limited-tunneling. Through fitting to this transport model, the size of conductive grain, the separation distance between two-grains, and the charging energy per grain in a single polyaniline nanofiber are estimated to be about 5 nm, 3 nm, and 78 meV, respectively. This nanotechnological approach has been applied to determination of mesoscopic charge transport in the polyaniline conducting polymer.

致謝

<div align="right">中華民國九十九年七月二十五日</div>

Contents

List of Figures

Chapter 1

Introduction

1.1 Overview

''It is a nano world, let's make it a better place'' [1]-there is a lot of truth in this cheerful slogan. Actually, if the scientific community ever needed to be convinced that nanotechnology was real, D. M. Eigler and E. K. Schweizer (They were working at IBM's Almaden Research Center in San Jose, California, United States) provided the evident indication in the 5 April 1990 issue of *Nature* [2]. They achieved a milestone in humankind's ability to build small structures by utilizing an ultra-high vacuum scanning tunneling microscope in liquid helium environment (~ 4 K). This ability was demonstrated to be able to move and position individual atoms on a metal surface with atomic-scale precision. In possibly the most well-known image in the history of nanotechnology, they wrote down the letters ''IBM'' with 35 xenon atoms on a smooth nickel surface. After this pioneering feat done, the field, nano world, was created.

Various structures of matter having dimensions of the order of a billionth of a meter manipulated and investigated by nanotechnology were preformed. In the past two decades, the diversity of inorganic structures with nanoscale sizes such

as nanowires (NWs) [3, 4], nanocrystals [5, 6], nanotubes [3, 7] and nanobelts [8] have been synthesized by using either chemical or physical strategy and give a great deal of opportunities for the assembly of nanoscale devices and arrays by the bottom-up approach. Organic materials with nanoscale structures have also been made [9]. Due to high surface-to-volume ratio, these nanoscale structures represent novel and / or enhanced functions crucial to many fields of technology. Hence, preliminary field-effect transistors [10], single electron transistors [11], light-emitting diodes [12], photo-detectors [13], chemical sensors [14], and logic gates [15] have been demonstrated immediately.

In a bulk material, electrons are free to move in the solid, so their energy spectrum is almost continuous and the density of electron state per unit energy increases as the square-root of energy. In contrast, from three-dimensional bulk system down to a one-dimensional nanostructure, electrons feel confined gradually and the continuous energy spectrum will become discrete and the energy gap will increase. Undoubtedly, in this situation, the fundamental problems in quantum mechanics, tunneling, phase interference and weak localization effects, play an important role in nanostructure materials, should be taken account of. For example, the electron-electron interactions in one-dimensional metals exhibit dramatically different behavior from three-dimensional metals, in which electrons form a Fermi liquid [16]. Because the electrostatic charging energy is inversely proportional to the grain size of material, the Coulomb blockage effect cannot be neglected in nanostructure materials and dominate the electron transport behavior [11]. Besides, as the dimensions are reduced to a length smaller than the electron's mean free path, the electronic transport becomes ballistic and the quantized conductance is observed [17].

In order to explore the electrical properties of these nanostructures, the

technique of the electron-beam lithography and focused-ion-beam deposition for two- [18, 19] or four- [20, 21] electrode fabrication has been used recently. The scanning probe microscopy for making contacts to these nanostructures is also adopted to address current-voltage characteristics studies [22, 23]. The nano world is already upon us. It cannot be questioned and refused. If we enter it with a positive attitude, it could help decorate and improve our life in the near future.

1.2 Outline of Work

The first portion of this work is presented in chapter 3. According to temperature dependence of resistance and current-voltage characteristic in two-probe ZnO NW devices, contact- and nanowire-dominated devices can be distinguished. A disorder system that occurs between metal-semiconductor interfaces is proposed to explain the transport behaviors of the contact-dominated devices. Besides, we demonstrate that two-probe electrical measurement can also be applied to the exploration on the intrinsic properties of nanowire. This two-probe measurement approach works on highly resistive nanowires without Ohmic contact issue, as well. By employing this method, the electrical resistivity and carrier concentration of ZnO, InP and GaP NWs have been investigated.

The second portion of this work is illustrated in chapter 4. We fabricate a series of two-probe InP NW devices. These NWs fabricated nanodevices are picked up from the same source intentionally. Based on the result in chapter 3, contact or NW-dominated InP devices can be separated each other. In the past it is believed that the electronic and optoelectronic properties of nanodevices are mainly governed by intrinsic NWs. Here contact- and NW-dominated nanodevices are used to expose to light (green laser) and gas (oxygen) to identify the influence of contact effect.

The third portion of this work is given in chapter 5. Besides inorganic nanostructure materials surveyed, PANI nanofibers have also been fabricated two-probe nanodevices and studied the intrinsic transport properties. The dielectrophoresis technique is adopted to facilitate to move and position nanofibers onto a nanogap. To shine the electron-beam on contact area, the organic/metal contact resistance is reduced in order to probe the intrinsic electrical properties of a single PANI nanofiber. Through deliberately discussions, the charge energy limited tunneling theory can be used to describe the transport properties of PANI nanofibers.

In chapter 2, we sketch theoretical models that can be applied to our work. Thermionic-emission theory, thermal activated transport, Mott variable range hopping and charge energy limited tunneling are followed to introduce briefly. Experimental results as well as discussions are presented in chapter 3 ~ 5 and the conclusions are summarized in chapter 6.

References

[1]   A. Nordmann, *Nano Researchers Facing Choices* 10, 13 (2007)

[2]   D. M. Eigler and E. K. Schweizer, *Nature* 344, 524 (1990)

[3]   J. Hu, T. W. Odom and C. M. Lieber, *Acc. Chem. Res.* 32, 435 (1999)

[4]   Y. Cui, X. Duan, J. Hu and C. M. Lieber, *J. Phys. Chem. B* 104, 5213 (2000)

[5]   C. B. Murray, C. R. Kagan and M. G. Bawendi, Science 270, 1335 (1995)

[6]   A. L. Gast and W. B. Russel, *Phys. Today*, 24 (1998)

[7]   S. Iijima, Nature 354, 56 (1991)

[8]   Z. W. Pan, Z. R. Dai and Z. L. Wang, *Science* 291, 1947 (2001)

[9]   J. Huang, S. Virji, B. H. Weiller and R. B. Kaner, *J. Am. Chem. Soc.* 125, 314 (2005)

[10] S. J. Tans, A. R. M. Verschueren and C. Dekker, *Nature* 393, 49 (1998)

[11] D. L. Klein, R. Roth, A. K. L. Lim, A. P. Alivisatos and P. L. McEuen, *Nature* 389, 699 (1997)

[12] Y. Cui and C. M. Lieber, *Science* 291, 851 (2001)

[13] H. Kind, H. Yan, B. Messer, M. Law and P. Yang, *Adv. Mater.* 14, 158 (2002)

[14] Y. Cui, Q. Wei, H. Park and C. M. Lieber, *Science* 293, 1289 (2001)

[15] V. Derycke, R. Martel, J. Appenzeller and P. Avouris, *Nano Lett.* 1, 453 (2001)

[16] M. Bockrath, D. H. Cobden, J. Lu, A. G. Rinzler, R. E. Smalley, L. Balents and P. L. McEuen, *Nature* 397, 598 (1999)

[17] H. Ohnishi, Y. Kondo and K. Takayanagi, *Nature* 395, 780 (1998)

[18] B. Wei, R. Spolenak, P. K. Redlich, M. Rühle and E. Arzt, *Appl. Phys. Lett.* 74, 3149 (1999)

[19] Y. F. Lin and W. B. Jian, *Nano Lett.* 8, 3146 (2008)

[20] T. W. Ebbesen, H. J. Lezec, H. Hiura, J. W. Beentt, H. F. Ghaemi and T. Thio,

Nature 382, 54 (1996)

[21] S. P. Chiu, Y. H. Lin and J. J. Lin, *Nanotechology* 20, 015203 (2009)

[22] H. Dai, E. W. Wong and C. M. Lieber, *Science* 272, 523 (1996)

[23] Y. C. Ou, J.J .Wu, J. Fang and W. B. Jian, *J. Phys. Chem. C* 113, 7887 (2009)

Chapter 2

Theoretical Models

Since semiconductor devices had to make contact with the outside world, the interface between metal and semiconductor had become vital. The metal-semiconductor junction formed either a rectifying or an Ohmic contact. In the beginning the metal-semiconductor junction theory will be illustrated in Section 2.1. The electrical transport theories about thermal activated transport (Section 2.2), Mott-variable range hopping (Section 2.3), charge energy limited tunneling (Section 2.4) are also introduced in the following paragraphs, since they could be well-applied to account for our experimental data.

2.1 Thermionic-emission Theory

The current transport in a metal-semiconductor (M-S) junction is due mainly to majority carriers as opposed to minority carriers in a *p-n* junction. When a metal makes contact with a semiconductor, a barrier is formed at M-S interface. This barrier is responsible for controlling the electrical properties. In 1942, Bethe proposed the thermionic-emission theory to accurately describe the electrical behaviors in M-S interface [1, 2]. In the below subsection, we will consider a metal makes contact with an *n*-type semiconductor and discuss the total current density.

The sum of current density J from the semiconductor to the metal $J_{S \to M}$ and from the metal to the semiconductor $J_{M \to S}$ can be given as the following form

$$
\begin{aligned}
J &= J_{S \to M} + J_{M \to S} \\
&= \left(\frac{4\pi e m^* k_B^2}{h^3} \right) T^2 \exp\left(-\frac{e\phi_B}{k_B T} \right) \exp\left(\frac{eV_a}{k_B T} \right) \\
&= \left[A^* T^2 \exp\left(-\frac{e\phi_B}{k_B T} \right) \right] \cdot \left[\exp\left(\frac{eV_a}{nk_B T} \right) \right] \cdot \left[1 - \exp\left(-\frac{eV_a}{k_B T} \right) \right]
\end{aligned} \tag{2.1}
$$

Eq. (2.1) can be written in a usual diode form as

$$
J = J_{ST} \exp\left(\frac{eV_a}{nk_B T} \right) \left[1 - \exp\left(-\frac{eV_a}{k_B T} \right) \right] \tag{2.2}
$$

, where
$$
J_{ST} \equiv \left[A^* T^2 \exp\left(-\frac{e\phi_B}{k_B T} \right) \right] \tag{2.3}
$$

e, m^*, n, k_B, h, ϕ_B and V_a are charge, effective mass of semiconductor material, ideality factor, the Boltzmann constant, the Planck constant, effective Schottky barrier height and applied bias, respectively. The effective Schottky barrier height, ϕ_B, is a function of applied bias which will decrease with an increase of the electric field. The parameter, A^* is called the effective Richardson constant for thermionic emission. The current-voltage characteristic of metal-semiconductor junction can be presented by a diode-like form such as a *p-n* junction, as shown in Eq. (2.2). In the forward bias (apply a positive voltage to the metal with respect to the semiconductor) the effective Schottky barrier is reduced and electrons can easily flow from the semiconductor into the metal. In contrast, in the reverse bias the

effective barrier height arise and electrons are limited to get a saturation current density, J_{ST}.

From Eq. (2.2) we could notice that ideality factor is an important parameter to determine whether this metal-semiconductor junction is a good diode or not. For an ideal mteal-semiconductor diode, the ideality factory, n, always keeps at unit. As values of V_a is greater than 3 k_BT / e, Eq. (2.2) can be represented in the simpler form

$$J = J_{ST} \exp\left(\frac{eV_a}{nk_BT} \right)$$
(2.4)

so that a plot of ln J versus V_a in the forward direction could give a straight line and the ideality factory could be extracted from the slop. Actually, we always measure the total current, I, rather than the current density, J. This is because that the determination of the current density necessitates an accurate measurement of the contact area, A. Hence, the advantage of retaining the more exact form of Eq. (2.4) is that a plot of $\ln\left[I / \left(1 - \exp\left(-eV_a / k_BT\right)\right) \right]$ versus V_a will give a straight line for all values of V_a, not only for the region V_a < 3 k_BT / e but also for negative value as well. The saturation current and the ideality factor could be drawn out from the intercept and slope in the plot of $\ln\left[I / \left(1 - \exp\left(-eV_a / k_BT\right)\right) \right]$ versus V_a, respectively.

As a general rule, the contact resistance, R_C, is inversely relative to the contact area, A, as

$$R_C = \frac{\rho_C}{A}$$
(2.5)

, where ρ_C is the specific contact resistivity. With the shrinking contact area, the

impact of contact resistance becomes more and more important to contribute enormously to the total resistance, especially in nanoscale metal-semiconductor devices. In order to comprehend the equivalent contact resistance in metal-semiconductor interface, we consider furthermore the differential form of Eq. (2.2). M-S contact results in the zero-bias specific contact resistivity of the form

$$\rho_C = \left(\frac{\partial J}{\partial V_a}\right)^{-1}\Bigg|_{V_a=0} = \left(\frac{k_B}{A^*Te}\right)\exp\left(\frac{e\phi_B}{k_BT}\right) \tag{2.6}$$

As shown in Eq. (2.6), the zero-bias specific contact resistivity will decrease rapidly as the effective Schottky barrier height decrease. The lower the barrier is, the smaller the contact resistance is. On the other hand, if the semiconductor has a higher doping concentration (N_d), the tunneling carriers will dominate the transport behavior, so Eq. (2.6) can then replace to be written as

$$\rho_C \propto \exp\left(\frac{\phi_B}{\sqrt{N_d}}\right) \tag{2.7}$$

which shows that the strong carrier concentration dependence of contact resistivity is observed.

2.2 Thermal Activated Transport

Using the Boltzmann approximation, the thermal equilibrium electron concentration in non-degenerated semiconductors can be defined as [3]

$$n = N_C \exp\left(-\frac{E_C - E_F}{k_BT}\right) \tag{2.8}$$

, where N_C, E_C and E_F are the effective density of states in the conduction band, the bottom edge of the conduction band and intrinsic Fermi level, respectively. We consider the total charge density in complete ionization condition. The net charge

10

density of semiconductor in thermal equilibrium should keep to be zero, indicating the total negative charges (electrons, n, and ionized acceptors, N_A^-) must be equal to the total positive charges (holes, p, and ionized donors, N_D^+). Hence, the charge neutrality condition is expressed as

$$n + N_A^- = p + N_D^+ \tag{2.9}$$

Consider the case of n-type semiconductor, where donor impurities with the carrier concentration N_D (cm^{-3}) are added into the material, the net charge equation can be re-written as

$$n = p + N_D^+ \approx N_D^+ \tag{2.10}$$

We apply Eq. (2.10) to Eq. (2.8), and then assume that $N_D > N_A$ (Compensated n-type material), the electron concentration can be approximated by

$$n \approx \left(\frac{N_D - N_A}{2N_A} \right) N_C \exp\left(-\frac{(E_C - E_D)}{k_B T} \right) \tag{2.11}$$

, where $E_A = E_C - E_D$ is an activation energy.

On the other hand, consider an external field applied E to semiconductor, the electric force will accelerate free electrons to create the current, called a drift current, J_{drift}. This drift current for n-type semiconductor can be given as

$$J_{drift} \simeq e\mu_n nE = \frac{1}{\rho} E \tag{2.12}$$

, where μ_n and ρ are the electron mobility and resistivity, respectively. Assume that the electron mobility is a weak temperature dependent parameter. Therefore, substitution of Eq. (2.11) into Eq. (2.12), the resistivity of n-type semiconductor, ρ, becomes

$$\rho = \rho_0 \exp\left(\frac{E_A}{k_B T} \right) \tag{2.13}$$

, where ρ_0 is a constant. The mathematical formula of Eq. (2.13) is called the thermal activated transport for semiconductor carriers. The thermal activated transport dominates the carriers behavior in semiconductors at sufficiently high temperatures.

2.3 Mott Variable Range Hopping

Mott first proposed in 1968 that the most frequent hopping process would not be a nearest state at low temperature and expected a temperature dependent resistance behavior which is called Mott variable range hopping (Mott-VRH) [4]. Mott variable range hopping transport is a model describing low temperature conduction in strongly disordered systems with localized states. The argument of this transport theory shows simply in the below.

We consider that at a temperature T the electron will normally hop to a site at a distance smaller than a hopping distance R. The hopping distances, R, is a function of temperature and increases with the decreasing temperature. Within a range R of a given site, the density of states per unit energy range near the Fermi energy is

$$\frac{4\pi}{3} R^3 g(E_F)$$

(2.14)

, where $g(E_F)$ is the density of states near the Fermi level and is assumed to be a constant in this model. Thus for the hopping process through a distance R with the lowest activation energy, the energy E will be the reciprocal of Eq. (2.14) and is given as

$$E = \frac{1}{\frac{4\pi}{3} R^3 g(E_F)}$$

(2.15)

When a hopping transport happens, electrons always try to find the lowest

activation energy state E and the largest hopping distance R. The hopping probability can be shown as

$$P \propto \exp\left(-2\frac{R}{\xi}\right) \cdot \exp\left(-\frac{E}{k_B T}\right)$$ (2.16)

, where ξ is the localization length. The hopping distance is much longer than the localization length at low temperatures. In order to take the maximum value of the hopping distance R, the first order of the differentiation of Eq. (2.16) to R will be considered

$$\frac{d}{dR}\left[\exp\left(-2\frac{R}{\xi}\right) \cdot \exp\left(-\frac{E}{k_B T}\right)\right]$$ (2.17)

The optimum value of R is

$$R = \left(\frac{9\xi}{8\pi k_B T g(E_F)}\right)^{1/4}$$ (2.18)

Because the resistivity, ρ, is inversely proportional to the hopping probability, so that we substitute for R into Eq. (2.16) to get the conductivity form

$$\rho \propto \exp\left[\left(\frac{T_0}{T}\right)^{1/4}\right]$$ (2.19)

, where

$$T_0 \propto \frac{1}{k_B \xi^3 g(E_F)}$$ (2.20)

Eq. (2.19) is called three dimensional Mott variable range hopping to describe the non-neighboring hopping process at low temperature. As a general rule, the Mott variable range hopping could be extended to a general formula as

$$\rho \propto \exp\left[\left(\frac{T_0}{T}\right)^{1/p}\right]$$ (2.21)

, where the exponent parameter p is 2, 3, or 4 for a one-, two-, or three-dimensional

disordered system, respectively. For other methods of deriving this equation (Eq. (2.21)), giving somewhat different value of T_0, please refer to Mott and Davis's [5] or Shklovskii and Efors's theory [6].

2.4 Charge Energy Limited Tunneling

The transport model of charge energy limited tunneling (CELT) is proposed in 1973 by P. Sheng and his co-worker for granular metals in which the conduction is supposed to proceed from tunneling between small conducting grains embedded in a insulating matrix [7, 8]. They predicted the temperature dependence of the low-field resistance,

$$R = R_{low} \exp\left(\left(\frac{T_0}{T}\right)^{1/2}\right) \tag{2.22}$$
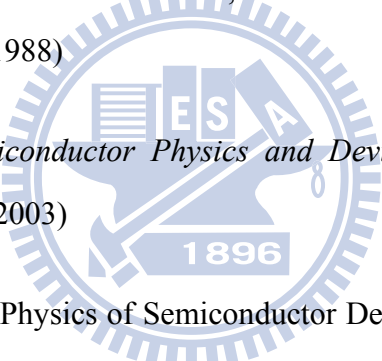
, where R_{low} and T_0 are constants. This equation can be attributed to a relationship $s \times E_C$ = constant, where s and E_C is the separation of neighboring metal grains and the charging energy, respectively. In Sheng model the charging energy, E_C, is an energy required to create a positive-negative charged pair to move an electron between two neutral conducting grains and is inversely proportional to the average diameter of the conducting grains, d (i.e. s / d = constant). In this regime (low-electric field) the voltage difference between neighboring granular metals is much smaller than $k_B T$ / e. Thermal activation is therefore the main mechanism responsible for charge generation. On the other hand, as the magnitude of electric-field is increased, an additional mechanism, field-induced tunneling, becomes more and more important and the charge carriers gradually deviates from the thermal equilibrium value. The field-induced tunneling mechanism can be written as

14

$$R = R_{high} \exp\left(\frac{E_0}{E}\right) \qquad (2.23)$$

, where R_{high} is a constant. E_0 high field approach.

In this model, the charging energy plays an important role. The generated carriers in a granular system are thermally assisted in the low-field regime and a field-induced in the high-field regime. Besides, tunneling only occurs between nearest neighboring grain.

References

[1] E. H. Rhoderick and R. H. Williams, *Metal-Semiconductor Contacts*, *2nd*; Clarendon press, Oxford (1988)

[2] D. A. Neamen, *Semiconductor Physics and Devices: Basic Principle*, *3th*; McGraw-Hill, New York (2003)

[3] S. M. Sze, K. K. Ng, Physics of Semiconductor Devices; John Wiley & Sons: Edison, New York (2005)

[4] S. N. Mott, *Conduction in Non-Crystalline Materials*; Clarendon Press; Oxford (1993)

[5] N. F. Mott and E. A. Davis, *Electronic Processes in Non-Crystalline Materialsls*; Clarendon Press; Oxford (1979)

[6] B. I. Shklovskii and A. L. Efros, *Electronic Properties of Doped Semiconductor*; Cardona (1984)

[7] P. Sheng, B. Abeles and Y. Arie, *Phys. Rev. Lett.* 31, 44 (1973)

[8]   B. Abeles, P. Sheng, M. D. Coutts, *Adv. Phys.* 24, 407 (1975)
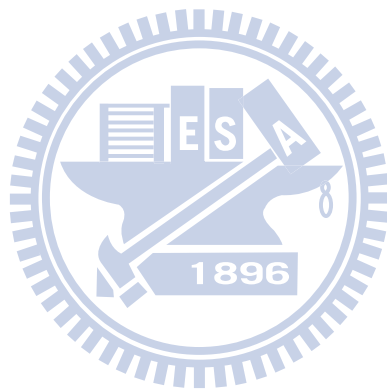
Chapter 3

Utilize Two-Probe Configuration Measurements to Survey the Impact of Nanocontact on Nanodevices and Transport Properties in Semiconductor Nanowires
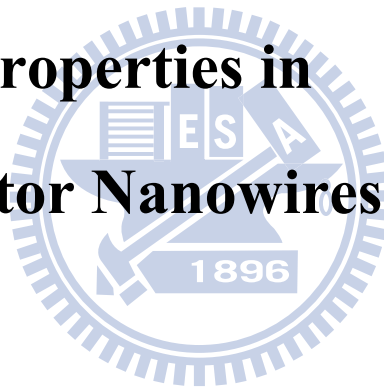
3.1   Introduction

Semiconductor nanowires (NWs) [1-3], nanocrystals [4, 6] and carbon nanotubes [7, 8], synthesized using either chemical or physical manners in the past decade, give us many opportunities for the assembly of nanoscale devices and arrays by the bottom-up approach. On account of high surface-to-volume ratio, these nanoscale materials represent novel and / or enhanced functions crucial to many fields of technology. Moreover, preliminary electronic and optoelectronic devices, such as field effect transistors (FETs) and light emitting diodes (LEDs) by utilizing nano

scale materials have also been perceptive and demonstrated successively [9, 10]. However, in order to exploit these to accomplish the high-dimensional, vertical integrated and multifunctional circuits in the near future, the contact problem in the nanoscale devices, plays the most important role, should be overcome, in particular, the most nanodevices possessing a two-probe configuration as the source and drain electrodes. Additionally, to identify and determine intrinsic properties of NWs also is a pivotal issue to touch the target of nanotechnology application.

An ideal interface between a nanowire and a metal contact in nanodevices is often assumed in many previous reporters. Actually, this is barely the case in reality due to the contact resistance. Recently it has been pointed out that the contact resistance should be taken into account when probing electrical transport in nanomaterials. Bachtold et al. applied four-probe electric measurements to carbon nanotubes and found the contact resistance could be reduced by six orders of magnitudes after electron beam exposure [11]. Hwang et al. discovered that the contact resistance is reduced as the Ti layer thickness, that is in the Ti/Au electrodes contacting on GaN NWs, is increased [12]. Zhang et al. proposed a model to describe contact-dominated behaviors at low field regime and to extract intrinsic nanowire resistivity at high field regime [13]. Furthermore, in order to eliminate a possible contamination layer formed between metal-semiconductor interfaces in nanoscale devices and to fabricate a good Ohmic contact to get the electrical properties in NWs, a rapid thermal annealing [14] or local current-induced Joule heating [15] were adopted.

In this work, a series of two-probe NW devices were fabricated to explore the current-voltage (*I-V*) characteristics and temperature dependence resistance. According to temperature behaviors of resistances, contact- and NW-dominated devices can be distinguished each other. In Section 3.3.1 only ZnO NW devices

were utilized to reveal the impact of nanocontact and a disordered contact picture between the nanowires and Ti/Au electrodes was proposed. In Section 3.3.2 ZnO, InP and GaP NW devices were investigated in determination of the intrinsic temperature dependent resistance.

3.2   Experimental Method

ZnO NWs were synthesized by a thermal evaporation (vapor transport) on quartz substrates with gold nanoparticles as catalysts to control the NW diameter [16]. InP and GaP NWs were synthesized by self-seeded, solution-liquid-solid growth [17]. NWs were analyzed by using a field-emission scanning electron microscope (FE-SEM, JEOL JSM-7000F). ZnO NWs are ~40 nm in diameter and 5-10 μm in length, whereas InP and GaP NWs are 2-5 μm in length and ~20 and ~30 nm in diameter, respectively. Prior to the electron-beam (e-beam) lithography process, micrometer-scale Ti/Au electrodes, current leads and alignment marks were photo-lithographically generated on a Si wafer (heavy doped p-type Si wafer), capped with a 400-nm thick SiO_2 layer, in order to prevent from current leakages through the substrate. In each experiment, the stocked ZnO, InP, or GaP NWs were dispersed on a pre-patterned substrate. FE-SEM was employed to locate the position of NWs. A standard e-beam lithography technique was used to pattern Ti/Au (40/150-nm thickness) current leads and to contact the NWs. The as-fabricated two-probe NW devices were annealed at 400 $^{\circ}$C in a high vacuum for 1 min in order to improve the contact.

All of as-fabricated two-probe NW devices were then placed into a crystat (Variable Temperature Insert Cryostat, CRYO Industries of America Inc.) for acquiring their temperature dependence of I-V measurements. These electrical characterizations were carried out with a current and voltage resolution of 10 pA

and 1 mV, respectively. The temperature dependent resistances reported in this article were measured in a temperature range between 300 and 77 K. Besides, it should be noticed that the resistance at a given temperature was extracted from the regime around the zero bias voltage.

3.3 Results and Discussion

A schematic diagram of our two-probe configuration NW devices is represented in Fig. 3.1 (a). The separation distance of ~ 1 µm between two e-beam lithography electrodes is kept the same for all of our nanodevices. FE-SEM image of a typical NW device is given in Fig. 3.1 (b) and the high-resolution FE-SEM image of the indicated rectangular area is depicted in Fig. 3.1 (c). The alignment marks are utilized for the e-beam lithography to determine the position of our randomly dispersed nanowires. In the below discussion, we will use the same configuration of nanodevices to investigate the impact of nanocontact (Section 3.3.1) and the transport behaviors of semiconductor nanowire (Section 3.3.2).
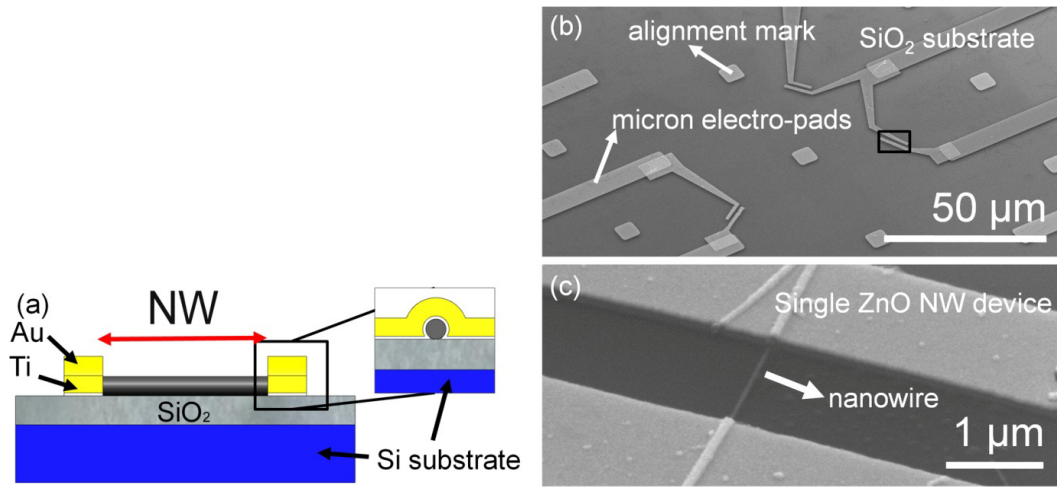
Figure 3.1: (a) A schematic diagram of a single NW device. Typically, the separation distance between the two contact electrodes is about ~1 μm. (b) FE-SEM image of a typical nanowire device with pre-fabricated micron electro-pads and alignment marks. An image of the indicated rectangular area is given in (c). The enlarged area displays a close view of a single ZnO NW device.

3.3.1 The Impact of Nanocontact on Nanodevices

In this work, more than thirty two-probe ZnO NW devices were fabricated to determine the intrinsic resistance of ZnO NWs and to explore the influence of nanocontact on nanodevices by analyzing their corresponding *I-V* characteristics and electron transport. It is emphasized that all of ZnO NWs used to fabricate nanodevices is detached from the same source sample. Even though this reason, we still observed a distinct RT (room-temperature) resistance of our ZnO NW devices. Hence, according to their RT (room-temperature) resistances and *I-V* curves, the devices were grouped into three different types. Fig. 3.2 (a) presents the first type, Type I, ZnO NW device with characteristics of a lower RT resistance, a linear *I-V*

demeanor in low voltage range, and a symmetrically downward bending feature in *I-V* curves. The low RT resistance and linear *I-V* dependence imply that both of the two nanocontacts are Ohmic type. Moreover, the temperature behavior of current at various bias voltage is analyzed with regard to the thermionic-emission theory (see Section 2.1) and shown in Fig. 3.2 (b) but we did not find any concordance. The result of inconsistence with Schottky contact supports the Ohmic type contacts for Type I devices as well. The circuit diagram of Type I devices with two Ohmic nanocontacts (indicated as circles) and one ZnO NWs (a resistance symbol) is given in the inset of Fig. 3.2 (a). Since both the two nanocontacts are Ohmic type, the device resistance could mainly come from the intrinsic ZnO NW resistance. On the other hand, the zero-voltage resistances as a function of temperature are displayed in Fig. 3.2 (c). The electron transport behavior can be well apprehended in agreement with the thermally activated transport (see Section 2.2) of electrons in ZnO NWs. The intrinsic ZnO NW resistance unveils thermally activated transport of conduction through the NW which conforms to our four-terminal measurements [18] and other groups' results [19, 20]. Since the conduction through the nanowire has been unambiguously investigated in Type I devices, the other devices having higher RT resistances could give electrical properties at nanocontact.

Figure 3.2: (a) *I-V* curves of a Type I ZnO NW device with a RT resistance of ~15 kΩ. The inset introduces a model of circuit diagram for Type I devices. (b) I/T^2 as a function of inverse temperature at various bias voltages. (c) Resistance as a function of temperature revealing electron transport in the Type I device.

A rectifying behavior on *I-V* curves, especially at low temperatures, has been unambiguously obtained and presented in Fig. 3.3 (a). We notice that the non-symmetrical *I-V* curves of the Type II NW device could only originate from one and only one Schottky nanocontact with the other one of Ohmic type. A circuit diagram model is offered in the inset of Fig. 3.3 (a) to depict the Schottky nanocontact, the ZnO NW, and the Ohmic nanocontact from left to right. The analyses in accordance with thermionic-emission theory (see Section 2.1) are given in Fig. 3.3 (b) and (c). For Type II devices, we observed linear dependence between $\ln(I/T^2)$ and $1/T$ with a slope indicating the effective Schottky barrier in the Schottky nanocontact. At a high bias voltage, the slope tends to zero which denotes

the vanishing of effective Schottky barrier ϕ_B when the bias approaches the break down voltage. Moreover, the *I-V* curve in a wide voltage range introducing in Fig 3.3(c) fits precisely with thermionic-emission theory both in forward and reverse bias voltages. Intriguingly and surprisingly, the ideality factor estimated from our fitting is very close to the ideal value of 1. Alternatively, the RT resistance of Type II devices ranges from near the upper bound RT resistance of Type I devices to that of Type III devices as will be acquainted in the next paragraphs. The temperature dependence of resistance $R(T)$ in Fig 3.3 (d) indicates that the electron transport behavior cannot be solely interpreted by the thermally activated transport in ZnO NW. In addition, We found that electron transport in these Type II devices departs from thermal activated transport and starts to reconcile with thermionic-emission and VRH conduction. We noticed that the fittings with either Schottky contact or VRH conduction do not make a significant difference at temperatures above 100 K. These results suggest that electrical properties, including *I-V* curves and zero-voltage resistances, mostly arise from the single Schottky nanocontact in the Type II NW devices.
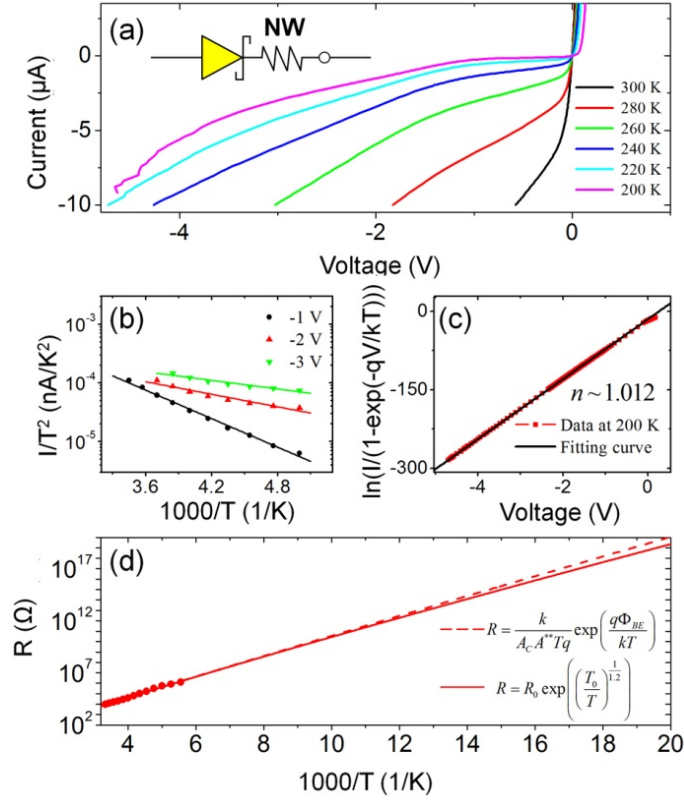
Figure 3.3: (a) *I-V* curves of a Type II ZnO NW device with a RT resistance of ~50 kΩ. The inset introduces a model of circuit diagram for Type II devices. (b) I/T^2 as a function of inverse temperature at various bias voltages. (c) $\ln(I/(1\text{-}\exp(\text{-}qV/kT)))$ as a function of voltage. (d) Resistance as a function of temperature revealing electron transport in this Type II device. The dashed and solid lines are best fittings (see text) of Equations 4 and 5, respectively.

Typical characteristics of the last type, the Type III ZnO NW devices with analyses through thermionic-emission theory are given in Fig. 3.4. First of all, the *I-V* curves in Fig. 3.4 (a) reveal symmetrical and an upward bending feature, and the data can be fitted well with thermionic-emission theory in reverse bias voltage. The linear dependence of $\ln(I/T^2)$ and $1/T$ at various bias voltage appears

prominently in Fig 3.4 (b) that supports our idea of Schottky contacts for Type III devices. Since no forward bias *I-V* reliance of a Schottky diode is spotted and the currents in both positive and negative voltages agree well with the reverse-bias thermionic-emission theory (see Fig. 3.4 (a) and (b)), we propose a model of two back-to-back Schottky contacts, which is commonly addressed to explain nonlinear *I-V* curves of semiconductor NW devices [21, 22], in the inset of Fig. 3.4 (a) to demonstrate the Type III devices. As for zero-voltage resistance, we obtained several different temperature dependent behaviors. Two typical sets of resistance data are presented in Fig. 3.4 (c) with the best fittings of dashed and solid lines following Schottky contact and VRH conduction, respectively. In this case, we found that the data points vary from the ideal Schottky contact form at temperatures below 200 K. Including the information of high RT resistances for Type III devices as well as the best fitting in accordance with VRH conduction form, we propose that a deteriorated contact between the Ti electrode and the ZnO NW forms due to a non-crystalline interface layer or titanium oxides. Owing to a diminished nanocontact area, a poor specific contact resistivity results in a high contact resistance and dominates electrical properties of the Type III NW devices.
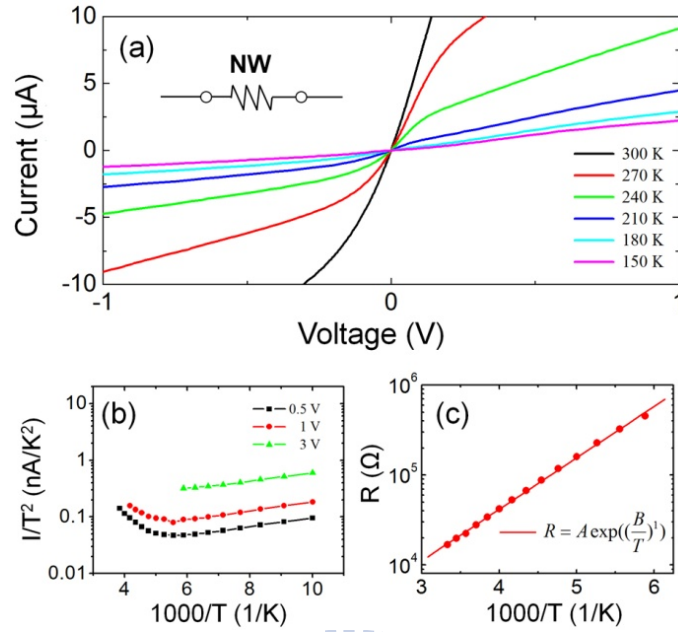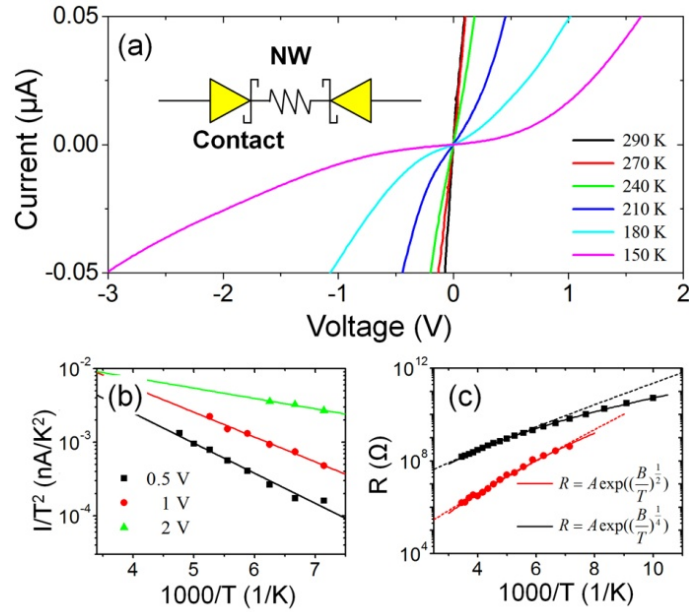
Figure 3.4: (a) *I-V* curves of a Type III ZnO NW device with a RT resistance of ~1.5 MΩ. The inset introduces a model of circuit diagram for Type III devices. (b) *I/T²* as a function of inverse temperature at various bias voltages. (c) Resistance as a function of temperature revealing electron transport in this Type III device (red circles) and in another Type III device having a RT resistance of ~128 MΩ (black squares). The dashed and solid lines are best fittings (see text) of Equations 4 and 5, respectively.

In order to discuss electron transport in ZnO NW devices and to fit their temperature dependent resistance, we adopted VRH conduction and included the exponent parameter *p* of 1 for thermally activated transport. The estimated exponent parameters as a function of device RT resistance are given in Fig. 3.5 (a). An unambiguous trend of a rising exponent parameter with an increase of RT resistance has been detected that signals worsened electrical properties in the nanocontacts. Moreover, the graph can be approximately separated into Regions A,

B, and C with an exponent parameter of about 1, 2, and bigger than 3, respectively. We discerned that all Type I ZnO NW devices are gathering in Region A indicating two Ohmic contacts on the individual ZnO NW. It is noted that the Type I devices have RT resistances lower than 100 kΩ. In addition, Type II devices distribute in Region B and unveil one-dimensional VRH conduction in one and only one nanocontact on the ZnO NW. Unlike Type I and II devices, Type III devices, having RT resistances higher than 100 kΩ, spread over Region B and C that connotes two- and three-dimensional VRH conduction in both nanocontacts of a NW device. In Fig. 3.5 (b) we provide three nanocontact models to elaborate our thoughts. Since a direct Ti metal contacting on ZnO should be attributed to Ohmic contacts as inferred from experiments of bulk systems [23], we propose a direct contacting model for nanocontacts of ZnO NW devices in Region A. Otherwise, the RT resistance is greater for devices in Regions B and C, we argue that titanium oxide form in the nanocontacts due to poor vacuum conditions during thermal evaporation. For NW devices in Region B, we believe that the oxide layer is thin enough for electrons to transport as one-dimensional VRH conduction. When the oxide layer is thick, the conduction channels mix to form two- and three-dimensional VRH conduction such as the proposed nanocontact model for devices in Region C.
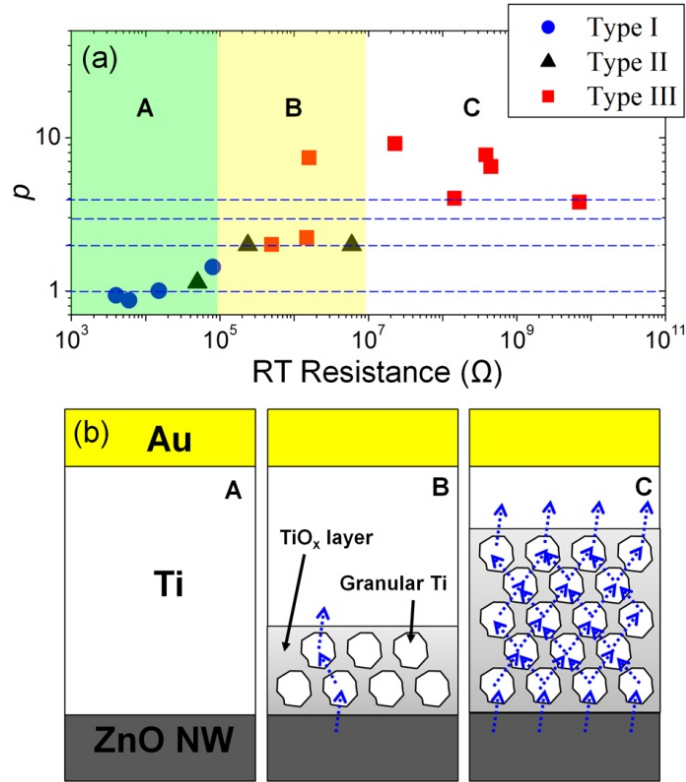
Figure 3.5: (a) The fitting exponent parameters *p* as a function of RT resistance for our as-fabricated ZnO NW devices of Type I, II, and III, marking as blue circles, black triangles, and red squares, respectively. The figure is approximately separated into Regions A, B, and C according to the exponent parameters of our devices. (b) Three different nanocontact models corresponding to the ZnO NW devices belonging to Regions A, B, and C of Figure (a).

In the above discussion, we have learned that the interface problems in nanowire-based electronics play important roles due to the reason that the reduced contact area in nanoelectronics multiplies enormously the contribution of electrical contact properties. In the interfacial nanocontact system, electron transport follows Mott variable range hopping theory of the form $R \propto \exp((T_0/T)^{1/p})$. Here, the

specific contact resistivity of an interfacial nanocontact system is further considered according to the form $\rho_C = R \times A_C$, where R and A_C represent RT resistance and contact area of nanodevices, respectively. The fitting exponent parameters, p, as a function of nanodevices contact resistivity at room temperature are given in Fig. 3.6. It should be emphasized that many two-probe nanodevices of different systems of semiconductor nanowires (The intrinsic electrical properties of these nanodevices will be illustrated in Sec. 3.3.2.) are used to extract the exponent parameters. A straightforward trend of a rising exponent parameter with an increase of specific contact resistance can be seen. The exponential parameter, p, rises from 2 to 4 with an increase of specific contact resistivity, as shown in Fig. 3.6, indicating a change from one- to three-dimensional hopping condition. Besides, a universal trend (i.e. the dashed line) is marked in Fig. 3.6, implying the nanocontact system seems to exhibit a general behavior of electron transport, even in these nanodevices fabricated by disparate nanowires. Moreover, the fitting exponent parameters as a function of T_0 also depict in the inset of Fig. 3.6. Since the fitting parameter, T_0, is proportional inversely to the localization length in disorder system (see Eq. (2.20)), the increasing T_0 suggests strongly a reduction of localization length as well as increasing disorder in the interfacial electron system.
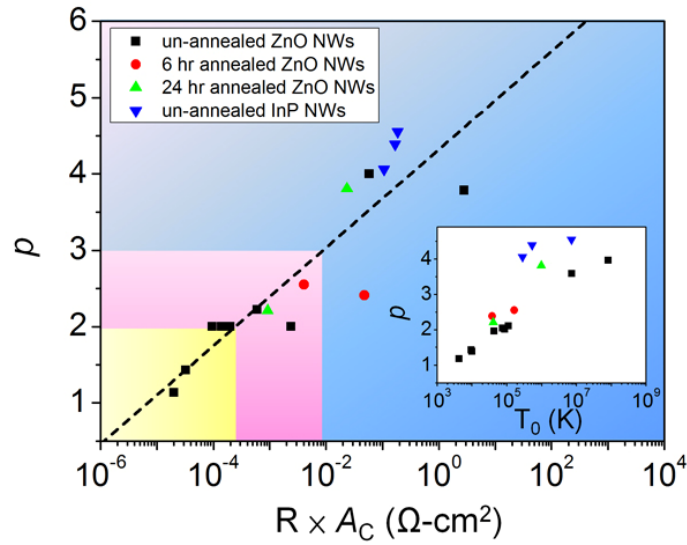
Figure 3.6: The fitting exponent parameters p as a function of RT contact resistivity for NW devices. The fitting exponent parameter as a function of T0 shows in the inset.

3.3.2 Transport Behaviors in Semiconductor

Nanonanowires

It is already learned in Section 3.3.1 that with the shrinkage of nanocontact area on nanodevices, the contact resistance will contribute extremely to the total resistance of the two-probe NW devices. In the below discussion, we have made the best efforts in facilitating the Ohmic contact so that the contact resistance can be neglected. Here, ZnO, InP, and GaP NW devices were investigated in determination of the intrinsic temperature dependent resistance.

Fig. 3.7 (a) displays a schematic diagram of a two-probe ZnO NW measurement system and the inset is a typical FE-SEM image of a ZnO NW device.

The scheme demonstrates that the NW was buried under the leads (electrodes) and contacted with a Ti metal, having a contact area of ~1×0.04 μm². The separation distance between two probes is a constant of ~1 μm. The targeted NWs were selected from the same source sample. Since these NWs have the same diameter and length, they should exhibit the same resistance. Fig. 3.7 (b) presents data collected from three two-probe devices in which the NWs were detached from the same source sample. It was observed that not only the room-temperature resistances on the three devices, ZnO-1, ZnO-2, and ZnO-3, are largely different (up to four orders of magnitudes), but their temperature behaviors are also disparate. According to above-mentioned assumption, that is, NWs of the same sample source should have defect concentration and resistances in the same order of magnitude, we propose that the higher resistance from ZnO-1 and ZnO-2 devices could be due to the nanocontact. This conjecture has been confirmed by current-voltage measurements which exhibit a nonlinear, non-Ohmic behavior [24]. As reported in previous section, the nanocontact can be treated as a disordered system and the electron transport in nanocontact follows a theory of Mott-VRH (More theoretical and experimental detail could be referred to Section 2.2 and Section 3.3.1, respectively)

$$R(T) = R_0 \exp\left(\left(\frac{T_0}{T}\right)^{1/p}\right) \tag{3.1}$$

where R and T are resistance and temperature, T_0 is a constant, R_0 is a weak temperature-dependent constant, and p is the exponent parameter. The dashed lines give the best fits to data in Fig. 3.7 (b) to derive the exponent p of 2 and 4 for ZnO-2 and ZnO-1 devices, respectively. The increase of room-temperature resistance as well as disorder in the nanocontact can raise the exponent parameter p from 2 to 4 and the nanocontact-constrained electron system from one- to

three-dimensional Mott-VRH.

On the other hand, if a device, such as ZnO-3, holds the lowest room-temperature resistance, it implies that the intrinsically electrical property of the NW and the temperature-dependent resistivity may follow a thermally activated transport equation

$$R(T) = R_0 \exp\left(\frac{E_A}{k_B T}\right) \qquad (3.2)$$

where R_0 is a constant, k_B is the Boltzmann constant, and E_A is the activation energy. The solid line in Fig. 3.7 (b) presents the best fit to the data of ZnO-3 device according to the thermally activated transport equation. The room-temperature resistance of ZnO-3 device is 16.8 kΩ and the length and diameter of the NW are 1 μm and 40 nm, respectively, resulting in a resistivity of ~0.002 Ω cm. Assuming that the electron mobility is 50 cm^2 V^{-1} s^{-1} [25], we can estimate the carrier concentration to be 10^{19} cm^{-3} at room temperature. At temperatures lower than 140 K, it is amazing to see that the temperature-dependent resistance deviates from the theoretically predicted values. Since a random distribution of native defects and a disorder are introduced, the electron transport in ZnO NWs, having a low carrier concentration, should follow Mott-VRH at very low temperatures. The resistance of ZnO-3 device agrees well with the three-dimensional Mott-VRH theory (the dashed line, $p = 4$) at temperatures lower than 140 K. To verify this conjecture, we adopted a four-probe measurement method (see Fig. 3.7 (c)) and confirmed that the intrinsic NW transport follows the three-dimensional Mott-VRH theory described in Eq. (3.1) with the exponent parameter $p = 4$. This result is in consistent with a determination reported recently [20]. As a consequence, the two-probe measurement with two Ohmic contacts and low resistance can be employed in acquiring carrier concentration and electron transport properties in ZnO NWs.

Furthermore, the source sample of ZnO-4 is different from that of ZnO-3 and the room-temperature resistivity and carrier concentration of ZnO-4 were evaluated to be 17 Ω cm and 10^{16} cm^{-3}, respectively. The carrier concentration of ZnO-4 NW is about three orders of magnitude lower than that of ZnO-3 NW. It should be pointed out that the ZnO NWs picked up from different source samples can exhibit extraordinarily discrepant resistivities and carrier concentrations, even though they are synthesized by the same growth method. The change in carrier concentrations among NWs picked up from different source samples is expected to come from varied concentrations of structure defects such as oxygen vacancies and Zn interstitials.
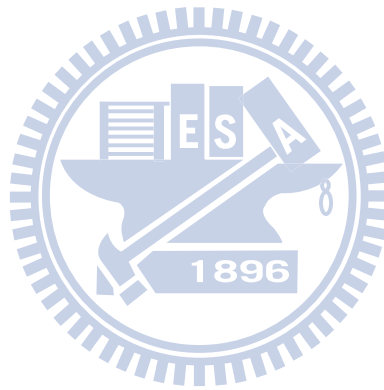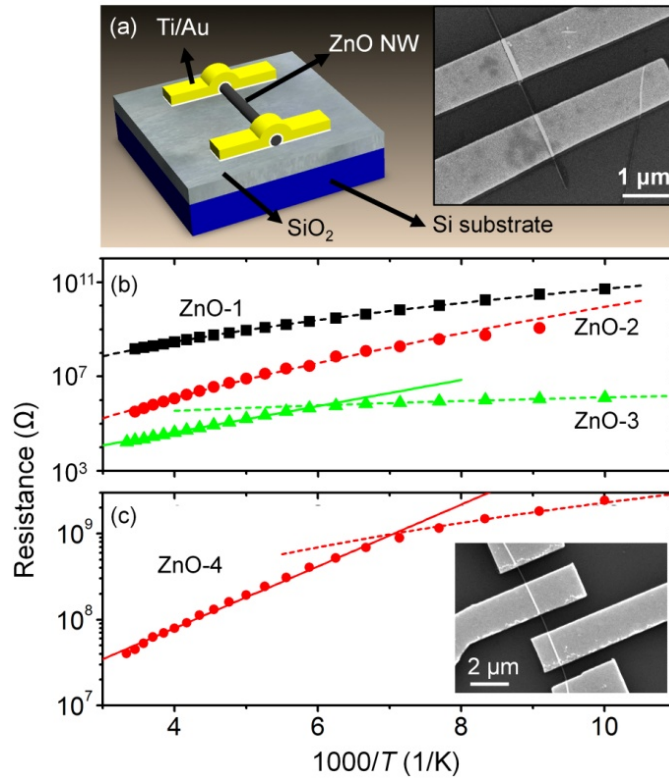
Figure 3.7: (a) Schematic diagram of a two-probe ZnO NW device with a typical SEM image shown in the inset. Temperature-dependent resistance of (b) two- and (c) four-probe ZnO NW devices. A schematic diagram of a four-probe device is drawn in the inset of Fig. (c). Solid and dashed lines delineate the best fits to the mathematical forms of thermally activated transport and Mott-VRH, respectively. After fitting to Mott-VRH (dashed lines), the exponents, p's, of ZnO-1, ZnO-2, ZnO-3, and ZnO-4 devices are estimated to be 4, 2, 4, and 4, respectively.

To extend the application of this two-probe measurement method to other semiconductor NWs, InP NW devices were fabricated through a solution-based growth[15] and a typical SEM image is presented in the inset of Fig. 3.8. InP NWs, like ZnO NWs, are natively *n*-type doped with a relatively low carrier concentration, which have been proved by the back gate effect (not shown in this

report). Fig. 3.8 illustrates temperature-dependent resistances of InP-1, InP-2, and InP-3 devices. The InP NWs were picked up from the same source but their room-temperature resistances, 1100, 420, and 30 MΩ for InP-1, InP-2, and InP-3 devices, varied considerably. Like ZnO-1 and ZnO-2 devices, the high resistance of InP-1 and InP-2 might be resulted from the nanocontact. The temperature behaviors at higher temperatures can be fitted by the thermally activated transport theory (Eq. (3.2), solid lines in Fig. 3.8), whereas those at temperatures lower than 150 K follow the Mott-VRH theory (Eq. (3.1), dashed lines). The exponent parameter p's are 2.4 and 4 for InP-2 and InP-1 devices, respectively, after fitting to Mott-VRH in a low temperature range. It is noted that the Mott-VRH theory can be solely used in fitting the data of ZnO-1 device in the whole range of temperatures, whereas both the Mott-VRH and thermally activated transport theories must be employed in fitting the data of InP-1 device. The difference comes from the NW resistance (resistivity). If the resistance (resistivity) of a NW is much lower, such as that of ZnO-3, the nanocontact resistance should dominate. Else, if they are comparable, the device characteristics will depend on contributions from both the NW and the nanocontact. Moreover, when thermally activated transport was used in fitting the data of InP NWs (InP-1, InP-2, and InP-3 devices) at high temperatures, the same slope of temperature-dependent resistance indicates the same activation energy (E_A) for carriers in InP NWs. On the other hand, since InP-3 device holds the lowest resistance, it implies an intrinsic electron transport in the InP NW. In the case of InP-3, the NW was ~1 μm in length and ~20 nm in diameter and the resistivity was determined as ~0.94 Ω cm. Assuming that the electron mobility is 1000 cm^2 V^{-1} s^{-1} [26], the carrier concentration at room temperature can be estimated as ~6.6×10^{15} cm^{-3}. The temperature-dependent resistance of InP-3 device indicates that electron transport at high temperatures can be well described by the thermally activated

36

transport theory, and at low temperatures it follows the three-dimensional Mott-VRH theory ($p = 4$). It should be emphasized that, in nanocontact-dominated devices such as InP-1 and InP-2, the exponent parameter p of Mott-VRH rises from 2.4 to 4 with an increasing room-temperature resistances of these InP NW devices. In contrast, in NW-dominated devices such as InP-3, the exponent parameter p of Mott-VRH remains as a constant of ~4, implying three-dimensional Mott-VRH in InP NWs.
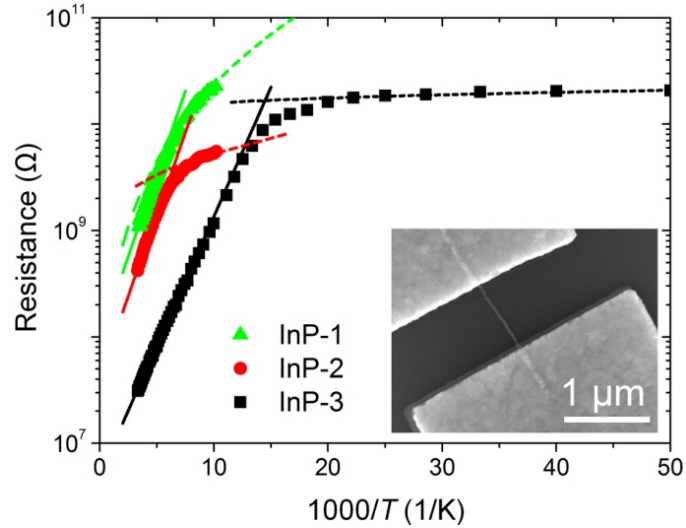
Figure 3.8: (a) Resistance as a function of inverse temperature for two-probe InP NW devices with a typical SEM image shown in the inset. The solid and dashed lines delineate the best fits to mathematical equations of thermally activated transport and Mott-VRH, respectively. After fitting to Mott-VRH (dashed lines), the exponents, p's, for InP-1, InP-2, and InP-3 are estimated to be 4, 2.4, and 4, respectively.

As mentioned above, it was observed that, as the NW resistance (resistivity) increases, the resistance of a two-probe NW device will be dominated by the

intrinsic NW resistance even though the contact is non-Ohmic and poor. We conclude, therefore, that ***the higher the NW resistance is, the easier the intrinsic electrical property of the NW can be drawn out***. As for a contact area of ~1×0.04 μm^2, the contact resistance is typically no bigger than ~1 GΩ. Thus, NWs of room-temperature resistance no less than 1 GΩ could easily be determined by using the two-probe technique. This idea has been materialized in GaP NWs. *I-V* curves of all GaP devices are displayed in Fig. 3.9. The inset is a temperature-dependent resistance of GaP-5. It is worth noting that the *I-V* curves of all devices are linear in a wide range of voltage (from -3 to 3 V). This behavior can be observed in devices of high-resistance nanostructures such as NWs and nanocrystals. If electron transport in GaP NW follows the thermally activated transport theory, the *I-V* should reveal an Ohmic characteristic of this NW rather than of hopping conduction in a disordered system of the nanocontacts. As expected, the temperature-dependent resistance, shown in the inset of Fig. 3.9, implies thermally activated transport. For example, GaP-5 which are 1 μm and 20 nm in length and diameter, respectively, exhibits a room-temperature resistance of 8.1 GΩ and a resistivity of ~254 Ω cm. Assuming that the electron mobility is 160 cm^2 V^{-1} s^{-1} [27], we can therefore estimate the carrier concentration as 1.53×10^{14} cm^{-3} at room temperature.
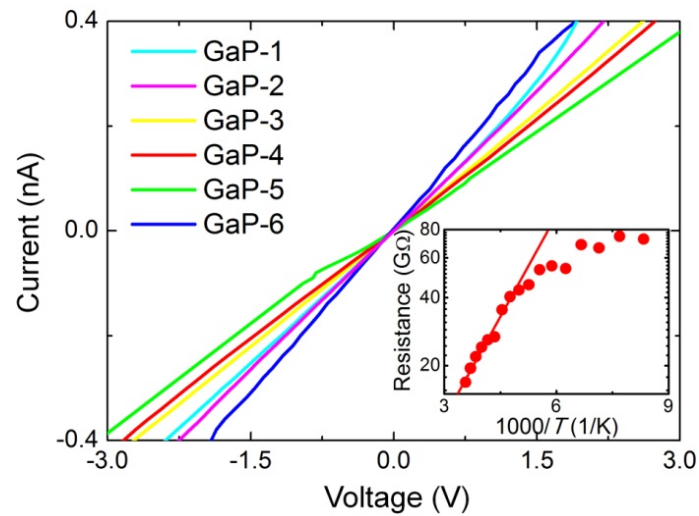
Figure 3.9: *I-V* curves, taken at room temperature, from six different GaP NW devices. The inset shows temperature-dependent resistance of GaP-5 device. The solid line in the inset demonstrates the best fit to the thermally activated transport equation.

References

[1]   J. Hu, T. W. Odom and C. M. Lieber, *Acc. Chem. Res.* 32, 435 (1999)

[2]   Y. Cui, X. Duan, J. Hu and C. M. Lieber, *J. Phys. Chem. B* 104, 5213 (2000)

[3]   H. Kind, H. Yan, B. Messer, M. Law and P. Yang, *Adv. Mater.* 14, 158 (2002)

[4]   D. L. Klein, R. Roth, A. K. L. Lim, A. P. Alivisatos and P. L. McEuen, *Nature* 389, 699 (1997)

[5]   U. Simon, *Adv. Mater.* 10, 1487 (1998)

[6] C. T. Black, C. B. Murray, R. L. Sandstrom and S. Sun, *Science* 290, 1131 (2000)

[7] S. J. Tans, A. R. M. Verschueren and C. Dekker, *Nature* 393, 49 (1998)

[8] H. Dai, E. W. Wong and C. M. Lieber, *Science* 272, 523 (1996)

[9] J. Wang, M. S. Gudiksen, X. Duan, Y. Cui and C. M. Lieber, *Science* 293, 1455 (2001)

[10] X. Duan, Y. Huang, Y. Cui, J. Wang and C. M. Lieber, *Nature* 409, 66 (2001)

[11] A. Bachtold, M. Henny, C. Terrier, C. Strunk, C. Schönenberger, J. P. Salvetat, J. M. Bonard and L. Forró, *Appl. Phys. Lett.* 73, 274 (1998)

[12] J. S. Hwang, D. Ahn, S. H. Hong, H. K. Kim, S. H. Hwang, B. H. Jeon and J. H. Choi, *Appl. Phys. Lett.* 85, 1636 (2004)

[13] Z. Y. Zhang, C. H. Jin, X. L. Liang, Q. Chen and L. M. Peng, *Appl. Phys. Lett.* 88, 073102 (2006)

[14] J. O. Lee, C. Park, J. J. Kim, J. Kim. J. W. Park and K. H. Yoo, *J. Phys. D: Appl. Phys.* 33, 1953 (2000)

[15] Y. Woo, G. S. Duesberg and S. Roth, *Nanotechnology* 18, 095203 (2007)

[16] W. B. Jian, I. J. Chen, T. C. Liao, Y. C. Ou, C. H. Nien, Z. Y. Wu, F. R. Chen, J. J. Kai and J. J. Lin, *J. Nanosci. Nanotechnol.* 8, 202 (2008)

[17] Z. Liu, K. Sun, W. B. Jian, D. Xu, Y. F. Lin and J. Fang, *Chem. Eur. J.* 15, 4546 (2009)
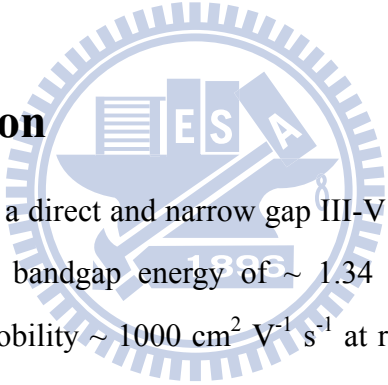
[18] Z. Y. Wu, I. J. Chen, Y. F. Lin, S. P. Chiu, F. R. Chen, J. J. Kai, J. J. Lin and W. B. Jian, *New. J. Phys.* 10, 033107 (2008)

[19] Y. W. Heo, L. C. Tien, D. P. Norton, B. S. Kang, F. Ren, B. P. Gila and S. J. Pearton, *Appl. Phys. Lett.* 85, 2002 (2004)

[20] P. C. Chang and J. G. Lu, *Appl. Phys. Lett.* 92, 212113 (2008)

[21] C. Y. Nam, D. Tham and J. E. Fischer, *Nano Lett.* 5, 2029 (2005)

[22] F. Hernandez-Ramirez, A. Tarancon, O. Casals, E. Pellicer J. Rodriguez, A. Romano-Rodriguez, J. R. Morante, S. Barth and S. Mathur, *Phys. Rev. B* 76, 085429 (2007)

[23] K. Ip, G. T. Thaler, H. Yang, S. Y. Han, Y. Li, D. P. Norton, S. J. Pearton, S. Jang and F. Ren, *J. Cryst. Growth* 287, 149 (2006)

[24] Y. F. Lin and W. B. Jian, *Nano Lett.* 8, 3146 (2008)

[25] P. C. Chang, C. J. Chien, D. Stichtenoth, C. Ronning and J. G. Lu, *Appl. Phys. Lett.* 90, 113101 (2007)

[26] E. D. Minot, F. Kelkensberg, M. van Kouwen, J. A. van Dam, L. P. Kouwenhoven, V. Zwiller, M. T. Borgstro1m, O. Wunnicke, M. A. Verheijen and E. P. A. M. Bakkers, *Nano Lett.* 7, 367 (2007)

[28] J. R. Kim, B. K. Kim, J. O. Lee, J. Kim, H. J. Seo, C. J. Lee and J. J. Kim, *Nanotechnology* 15, 1387 (2004)

Chapter 4

Enhanced Photoresponse and Gas Sensing of InP Nanowire Device

4.1   Introduction

Indium phosphide (InP) is a direct and narrow gap III-V group semiconductor with a room-temperature (RT) bandgap energy of ~ 1.34 eV [1]. InP possessing a relatively high electron mobility ~ 1000 cm^2 V^{-1} s^{-1} at room temperature [2], with respect to the more common semiconductor such as silicon and gallium arsenide, is a suitable candidate to make modern communications and high-frequency electronic devices. Moreover, due to a lattice match, InP used as a substrate for the development of long-wavelength optoelectronic devices has been manifested. Latterly, by using laser-assisted catalytic growth [3], *n*- and *p*-type doped InP materials have been transferred to form quasi-one-dimensional nanowires (NWs). It was then pointed out that InP NWs as building blocks could be applied to realize a sensitively polarized photodetection [4] and a light-emitting diode [5]. InP NWs were also exercised as a spacer and barrier in InAs NWs for observation of a single-electron tunneling effect [6]. Schottky diode based on a single InP

nanoneedle has also been demonstrated [7]. Most recently, it was presented in a theoretical prediction that, using an appropriate surface passivation, InP NWs might be applied as a gas sensor [8]. Until now electrical properties of InP NWs have not been broadly studied, in particular the understanding of temperature dependent resistance and current-voltage (I-V) behaviors. Most of nano electronic devices possess two-probe configuration as the source and drain electrodes so that intrinsic behaviors in NWs and contact resistance always cannot be distinguished explicitly [9]. In this work, we report a series of systematical experiments to explore the electrical properties in more than thirty InP NW devices with two-probe electrical configurations. The NWs for device fabrication are picked up from the same source sample. According to temperature behaviors of resistances in InP NW devices, contact- and NW-dominated devices could be separated each other. The electron transport and carrier concentration of native doping in InP nanowires can be determined. Furthermore, contact- and NW-dominated two-probe nanodevices are exposed to light (green laser) and gas (oxygen) to identify the influence of contact effect.

4.2   Experimental Method

InP NWs were synthesized by employing self-seeded, solution-liquid-solid growth and then stored in toluene. The detail of preparation method was described elsewhere [10]. As-synthesized InP NWs were characterized by utilizing field-emission scanning electron microscopy (FE-SEM, JEOL JSM-7000F) and transmission electron microscopy (TEM, JEOL JEM-2010F) to examine the morphology and diameters. The InP nanowire solution was diluted and then dropped onto a heavily doped p-type silicon substrate, which was capped with a 400-nm thick SiO_2 layer and photolithographically patterned with Ti/Au (~10/60

nm thickness) micro electrodes. To remove unintentional contamination from the surface of dispersed InP NWs, the substrate was heated at 150 $^\circ$C for 12 h in a high vacuum ambient. FE-SEM was utilized to local the position of NWs and two Ti/Au (~20/100 nm thickness) nanoscale electrodes, served as two-probe electrical configuration in InP NW devices, were followed to deposit in connection with the pre-patterned micro electrodes by using a standard e-beam lithography and a thermal evaporation method. The separation distance between two electrodes was kept at a constant for all InP NW devices. As-fabricated two-probe InP NW devices were annealed at 400 $^\circ$C for 1 min in a high vacuum ambient to make more conducting contact before they were placed in an insert liquid-nitrogen cryostat for the evaluations of temperature dependent I-V curve measurement. On the other hand, NW devices were also exposed under either a green-light laser (a wavelength of ~ 532 nm, a power of ~ 20 mW and spot size are of ~ 2 × 2 mm^2) or oxygen gas (1 atm; 99 % O$_2$) environment at room temperature to record the response and recovery characteristics and then clarify the intrinsic nanowire and the contact effect.

4.3   Results and Discussion

A TEM image of as-synthesized InP NWs, observed to be not only no evident aggregations but also almost straight shapes, is displayed in Fig. 4.1 (a). Without any catalyst seeds are extra seen at the tip of InP NWs. The distribution of InP nanowire diameters determined in TEM images is estimated and presented in the inset of Fig. 4.1 (a). The size distribution can be fitted with Gaussian distribution, yielding an average diameter of ~ 21.4 nm and a standard deviation of ~ 13.5 nm. Besides, as-synthesized InP NWs possess 2 ~ 5 μm in length. Due to the large diameter and long length of as-synthesized InP NWs, quantum confinement effect

can be excluded in the below discussion. Fig. 4.1 (b) illustrates a typical FE-SEM image of a single InP nanowire embedded in two Ti/Au electrodes. The distance separating the two Ti/Au electrodes contacted to an InP NW is ~ 1 μm. A cartoon schematic for our two-probe InP NW devices is represented in the inset of Fig. 4.1 (a).
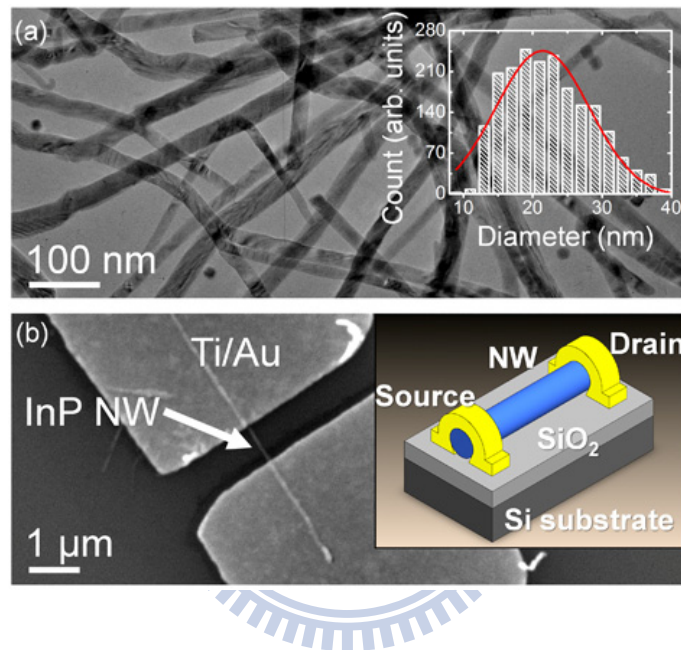
Figure 4.1: (a) TEM image of as-synthesized InP NWs with the size distribution and a red curve fitted according to a Gaussian function, shown in the inset. The average diameter and the standard deviation of nanowires are evaluated to be about 21.4 and 13.5 nm, respectively. (b) FE-SEM image of a single InP NW embedded in two Ti/Au electrodes. A cartoon schematic for our two-probe InP NW device is illustrated in the inset.

Fig. 4.2 (a) displays a typical temperature dependence of *I-V* characteristic of an InP NW device with a RT resistance about 22 MΩ. The black and light-blue curves represent the *I-V* behavior at 300 and 100 K, respectively. The current is

observed to arise with increasing voltage within the applied current range of ± 1 nA at variable temperature from 300 to 100 K. The *I-V* curve at room temperature reveals a linear and symmetric relationship that is also noticed in all of our InP NW devices, even though they have a striking variance in RT resistances. By analyzing the *I-V* characteristics of InP NW devices, the resistance at a given temperature can be determined from the regime around the zero-bias voltage. Fig. 4.2 (b) illustrates temperature dependent resistances of InP NW devices (NW-1 ~ NW-6). Although NWs fabricated nanodevices are taken out from the same source sample, their RT resistances, 4662, 931, 650, 530, 321 and 87 MΩ for NW-1, NW-2, NW-3, NW-4, NW-5 and NW-6 nanodevices, alter fairly enormous. It is suggested that the difference of RT resistances, which is up to two orders of magnitude, comes from the unavoidable contribution of contact resistance in two-probe configuration nanodevices [9]. Thermally activated transport (solid lines) can be used well in fitting the data at higher temperature regime, whereas the data at lower temperature regime follow the Mott-VRH transport theory (dashed lines), as depicted in Fig. 4.2 (b). The data at lower temperatures gradually deviate from the thermally activated transport to Mott-VRH conduction, implying that carrier transport is progressively govern by electron hopping through the disorder system, such as a deteriorated interface formed between the Ti/Au electrode and NW. The transition temperature as a function of RT resistance is plotted in the inset of Fig. 4.2 (b). The contact resistance and InP NW resistance have to be comparable and they will donate to the total resistance of the two-probe NW devices. We conclude that the higher RT resistance of InP NW devices is, the more contact resistance dominates. The detail explanation of temperature dependent behaviors has been demonstrated elsewhere [11]. Since the data at higher temperature mainly are described to follow the thermally activated transport, the activated energy in InP NWs could be extracted

from the slope of the plot of temperature dependent resistance to be about ~ 50 meV, ascribed possibly to the phosphorus deficiency related defect [12, 13]. Furthermore, the carrier concentration is also evaluated to be ~ 10^{15} cm^{-3} in the InP NW-dominated devices with the lowest RT resistance (NW-6). Temperature dependent resistances in InP NW devices facilitate us to distinguish both the contact and NW-dominated devices. Additionally, such a lower concentration in semiconductor materials gives rise to a promising perspective to develop nanoscale optoelectronics.
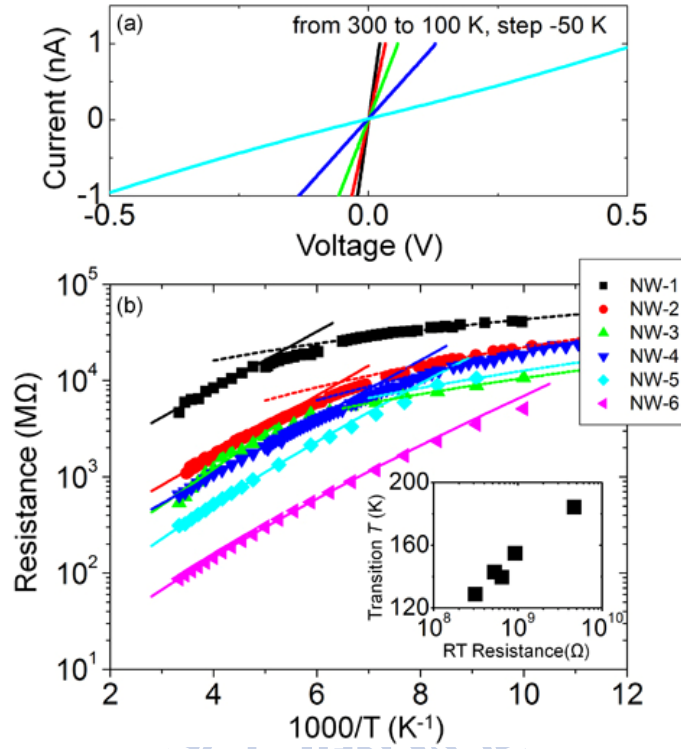
Figure 4.2: (a) *I-V* curves of a typical InP NW device with a RT resistance of ~ 22 MΩ. (b) Resistance as a function of inverse temperature for two-probe InP NW devices. The solid and dashed lines delineate the best fits to the mathematical equations of thermally activated transport and Mott-VRH, respectively. The inset shows the transition temperature as a function of RT resistance for InP NW devices.

To extend the result in determination of the contact- or NW-dominated devices and to understand further the impact of nanocontact on optoelectronic devices, the real-time response of InP NW devices to either light (green-light laser) or gas (oxygen) exposures have been studied. Fig. 4.3 (a) exhibits that the contact- or NW-dominated devices unveil distinct sensitive response to a green-light laser exposure at room temperature in an open air environment. The sensitivity is calculated in terms of the ratio of R / R_0, where R_0 and R denote the NW device

resistances before and after exposure, respectively. The R_0's of the contact-dominated device is 4.6 GΩ, whereas it is only 87 MΩ for the NW-dominated device. It is manifestly found that the contact-dominated device always exhibits a much higher ratio in comparison with the NW-dominated device. The data in Fig. 4.3 (a) delineate that almost recoverable curve in either contact or NW-dominated devices after the light exposure is removed, indicating that photo response is significantly larger than any thermionic or thermoelectric effects that might arise from a light-induced temperature increase. On the other hand, the response ratio, $\Delta R / R_0 = |R - R_0| / R_0$, as a function of RT resistance for our two-probe InP NW devices is given in Fig. 4.3 (b). Interestingly, an unambiguous trend of a rising response ratio, $\Delta R / R_0$, with the increase of RT resistances for InP NW devices has been monitored. The response ratio of NW-dominated devices with a RT resistance lower than 10^2 MΩ is only 10 ~ 20 %, whereas that of contact-dominated devices with a RT resistance close to 10^4 MΩ almost gets up to 50 % addition in response to the light exposure. Actually, for the photo response, it is well-known that a variation of resistances under light illumination is mainly due to the increase in the number of carriers in semiconductors. For example, in a direct bandgap semiconductor, such as InP, the photo energy absorption is a process that requires no any assistance from lattice vibrations. As the photo energy is absorbed, free electron-hole pairs (EHPs) will be generated in the inner of semiconductor materials. As an electric field applies to semiconductors, these EHPs generated will then be separated and accelerated in opposite directions to contribute carriers and diminish resistances. We conjectured that, in contact-dominated devices, most of carriers are limited not to pass through a barrier existing in metal-semiconductor interface. However, while a light with efficient energy exposes to contact-dominated devices, extra carriers with higher energy will be generated by

the incident light and then reduce the barrier height. The distorted barrier permits more tunneling carriers across so that an enhanced photo response ratio can be observed. This observation in contact-dominated devices is consistent with previous reports where a higher photo response has been demonstrated due to a modified Schottky barrier [14-16].

Figure 4.3: (a) The sensitivity of light exposure for contact and NW-dominated two-probe InP NW devices. (b) The response ratio (ΔR / R_0) as a function of RT resistance for two-probe InP NW devices.

Fig. 4.4 (a) exhibits that the contact- or NW-dominated devices unveil distinct response to oxygen exposure at room temperature. The R_0's of the contact- and NW-dominated devices are 692 and 28 MΩ, respectively. It is surprising that the contact-dominated device also illustrates a much higher ratio of resistance changes, showing a marked contrast to the NW-dominated device. Unlike the light exposure to InP NW devices, the sensitivity with increasing time of oxygen exposure reflects

a gradually elevated behavior and the response time (i.e. the rise and decay time) of oxygen exposure is very blunt to be larger than 12 h. Indeed, the principle of charge transfer between a nanostructure and its surface-adsorbed species has been unfolded to explain the response behaviors in various gas sensors. As InP NW is exposed to oxygen gas, oxygen gas will adsorb on the surface, leading to a formation of surface species, such as In_2O_3 or P_2O_5 [17]. The adsorbed species on InP NW surface act as electron acceptors generating an electron-depleted surface layer. As a result, the resistance increases. This discovery is for the first time to observe the oxygen response in InP NW. Meanwhile, the response ratio as a function of RT resistance for two-probe InP NW devices is also given in Fig. 4.4 (b). Since the separation distance between two electrodes was kept a constant and all NWs fabricated devices had a uniform diameter, the area of NW devices to expose oxygen gas is always the same so that the number of adsorbed oxygen on the surface of InP NW devices is the same. With the increase of RT resistances for InP NW devices, the contact resistance gradually governs the carrier transport, indicating an equivalent barrier forms between metal-semiconductor interfaces and the resistances progressively increase. Hence, it is unearthed clearly the contact-dominated devices display a higher response ratio, as shown in Fig. 4.4 (b).
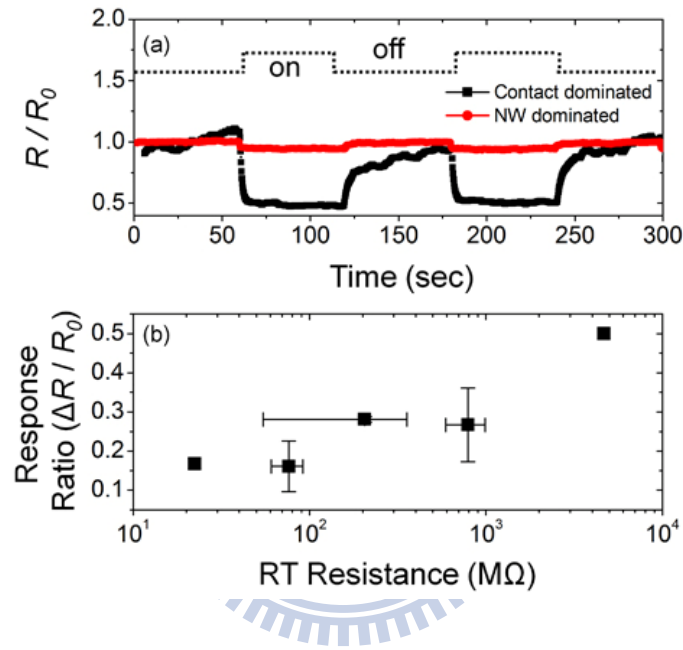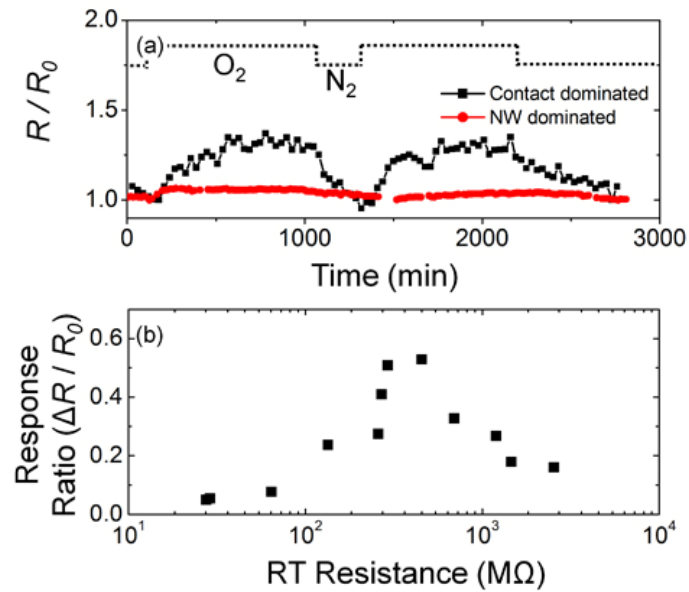
Figure 4.4: (a) The sensitivity of oxygen exposure for contact- and NW-dominated two-probe InP NW devices. (b) The response ratio ($\Delta R / R_0$) as a function of RT resistance for two-probe InP NW devices.

References

[1]   L. Pavesi, F. Piazza, A. Rudra, J. F. Carlin and M. Ilegems, *Phys. Rev. B* 44, 9052 (1991)

[2]   S. M. Sze, K. K. Ng, Physics of Semiconductor Devices; John Wiley & Sons: Edison, New York (2005)

[3]   M. S. Gudiksen, J. Wang and C. M. Lieber, *J. Phys. Chem. B* 105, 4062 (2001)

[4]   J. Wang, M. S. Gudiksen, X. Duan, Y. Cui and C. M. Lieber, *Science* 293, 1455 (2001)

[5] X. Duan, Y. Huang, Y. Cui, J. Wang and C. M. Lieber, *Nature* 409, 66 (2001)

[6] C. Thelander, H. A. Nilsson, L. E. Jensen and L. Samuelson, *Nano Lett.* 5, 635 (2005)

[7] T. Strupeit, C. Klinke, A. Kornowski and H. Weller, *ACS Nano* 3, 668 (2009)

[8] M. D. Moreira, P. Venezuela and T. M. Schmidt, *Nanotechnology* 19, 065203 (2008)

[9] Y. F. Lin and W. B. Jian, *Nano Lett.* 8, 3146 (2008)

[10] Z. Liu, K. Sun, W. B. Jian, D. Xu, Y. F. Lin and J. Fang, *Chem. Eur. J.* 15, 4546 (2009)

[11] Y. F. Lin, T. H. Chen, C. H. Chang, Y. W. Chang, Y. C. Chiu, H. C. Hung, J. J. Kai, Z. Liu, J. Fang and W. B. Jian, *Phys. Chem. Chem. Phys.* accepted (2010)

[12] A. P. Seitsonen, R. Virkkunen, M. J. Puska, R. M. Nieminen, *Phys. Rev. B* 49, 5253 (1994)

[13] G. Marrakchi, K. Cherkaoui, A. Karoui, G. Hirt and G. Müller, *J. Appl. Phys.* 79, 6947 (1996)

[14] R. R. Mehta and B. S. Sharma, *J. Appl. Phys.* 44, 325 (1973)

[15] N. Matsuo, H. Ohno and H. Hasegawa, *Jpn. J. Appl. Phys., Part 2* 23, L299 (1984)

[16] O. Katz, V. Garber, B. Meyler, G. Bahir and J. Salzman, *Appl. Phys. Lett.* 79, 1417 (2001)

[17] G. Hollinger, E. Bergignat, J. Joseph and Y. Robach, *J. Vac. Sci. Technol. A* 3. 2082 (1985)

Chapter 5

Nano Approach Investigation of Conduction Mechanism of Polyaniline Nanofibers

5.1   Introduction

Similar to the revolutionary miniaturization in electronic industry began in 1950s, flexible electronics might also change the world in the near future [1, 2]. Organic conducting material is a promising material to offer opportunities in developing flexible electronics. A great amount of theoretical and experimental works in organic conducting material were reported when the first highly doped conjugated polymer, polyacetylene, was discovered to manifest a dramatic decrease in its resistivity via halogen treatment in 1977 [3]. Among all the conducting polymers, Polyaniline (PANI) is one of the potential synthetic metals due to its low-cost synthesis, fast processability, and environmental stability in either the doped conducting or the de-doped insulting form. The applications of PANI, such as chemical sensors [4], field effect transistor [5], and memory devices [6], have been

demonstrated as well. Very recently, PANI nanostructures have been synthesized by using the template-free or template synthesis so as to raise the surface/volume ratio and to enhance the sensitivity in comparison with that of their bulk [4, 7]. Despite the abundant achievements in applied aspects, there are still a lot of controversial issues in the fundamental conduction mechanism of the conducting PANI for a long time. In this study, PANI nanofibers were synthesized by using polymerization method and their electrical transport was carried out.

5.2   Experimental Method

Polyaniline nanofibers were synthesized by using a rapidly mixed reaction [8]. A description of the synthesis method is given as follows. A solution of ammonium persulfate (0.183g, 0.8 mmol, >99%, Sigma-Aldrich Ltd.) dissolved in 10 mL of 1M HCl was carefully poured in a solution of aniline (0.298 g, 3.2 mmol, >99%, Sigma-Aldrich Ltd.) dissolved in 10 mL of 1M HCl. The mixed solution was stirred immediately at room temperature. The polymerization began and the mixed solution had turned to deep green color. This solution was stirred continuously for 24 hours. To store polymer solution, 0.5 mL of this solution was fetched and diluted with distilled water of 10 mL. Polyaniline nanofibers were stocked in the water solution. The schematic diagram for the synthesis of PANI nanofibers was illustrated in Fig. 5.1. Dimensions and morphology of polyaniline nanofibers were all recorded by using high-emission scanning electron microscopy (FE-SEM, JELO JSM-7000F).

Micrometer-scale Ti/Au (~10/60 nm thickness) electrodes were made by means of conventional photolithography on Si substrates, which were capped with a 400-nm thick SiO_2 layer, in order to prevent from any possible contribution of current leakage through the substrate. The as-synthesized polyaniline solution was

protonated (deprotonated) to doped (dedoped) form by washing it with 0.25M HCl (0.2M $NH_3 \cdot H_2O$) solution. Several drops of the doped, as-synthesized, and dedoped polyaniline solutions were deposited onto the pre-patterned Si substrate and then were dried at room temperature in air to get thin-film devices. On the other hand, the standard electron-beam lithography technique was adopted to define two submicrometer-scale Ti/Au (~20/100 nm thickness) current leads with a gap of 150-300 nm in width between them, connecting to the pre-patterned micrometer-scale electrodes of Si substrates. Before polyaniline nanofibers were positioned into the gap, the resistance of the gap at room temperature was inspected to be an order of magnitude much higher than 1 TΩ. The high resistance guaranteed that a good insulation existed between two current leads so as to detect the intrinsic electrical properties of the polyaniline nanofibers after positioned into the gap. Several drops of the as-synthesized polyaniline solutions were introduced to put on the gap substrates and a dielectrophoresis technique with a sinusoidal wave at a frequency of 1 MHz was applied across the two current leads for 3 min to move and position the nanofibers into the gap. In the dielectrophoresis procedure, the alternating voltage was selected in the range of 3 to 6 V, depending on the separation distance of the gaps. Besides, a series capacitor of 10 μF was placed in the equivalent circuit to filter out any direct current component and to avoid electrochemical reactions. Subsequently, the drop of solution was gently blown off the substrate with a stream of dry nitrogen gas. The as-fabricated nanofiber devices were exposed to electron beam with a dose of 3×10^4 C/m^2 s for 1 h, especially at the contact area between the current lead and the nanofiber, to reduce the device resistance. The two respective procedures to fabricate PANI nanofiber thin-film and nanoscale devices are revealed briefly in Fig. 5.2.

All of the thin-film and nanofiber devices were located in a cryostat (Variable

Temperature Insert Cryostat, CRYO Industries of America Inc.) with helium gas (>99.99 %) at a pressure of 760 Torr for acquiring temperature dependence of two-probe electrical properties. The current-voltage characteristics were performed by using an electrometer with a current resolution of 10 pA and a voltage resolution of 1 mV. The standard deviation of the estimated resistance around the zero bias voltage at a given temperature was less than 0.1 %. The transport properties were determined at temperatures ranging from 300 down to 80 K.
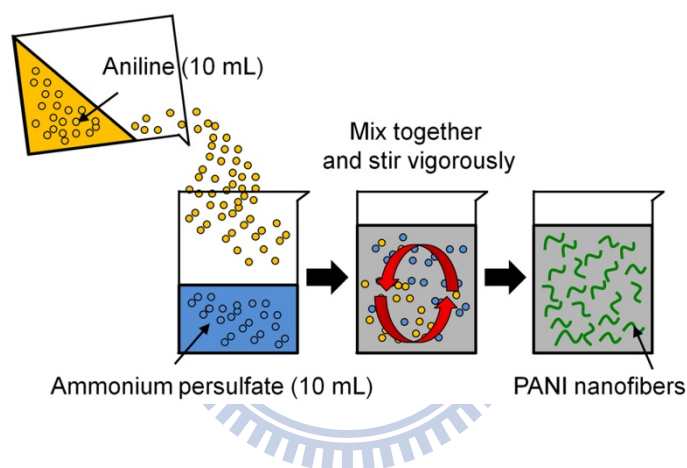
Figure 5.1: A schematic illustration of polyaniline nanofibers synthesis in a rapidly-mixed reaction.
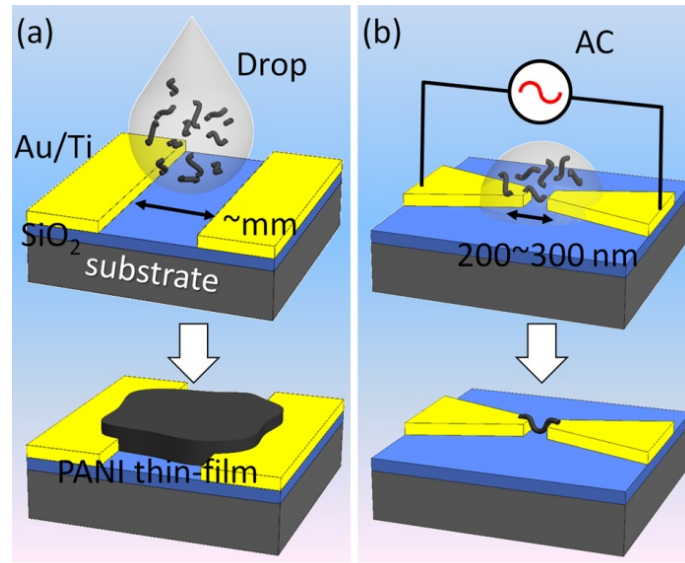
Figure 5.2: Schematic diagrams outlining the fabrication procedure of (a) polyaniline nanofiber thin-film device and (b) nanoscale nanodevices.

5.3   Results and Discussion

The as-synthesized PANI nanofibers, as displayed in Fig. 5.3 (a), are unfolded entangled appearances. The length of PANI nanofibers is observed to be at most in the range of several hundreds of nanometers. The distribution of PANI nanofiber diameters determined in FE-SEM image is estimated and presented in the inset of Fig. 5.3 (a). The size distribution can be fitted with Gaussian distribution, yielding an average diameter of ~ 45.0 nm and a standard deviation of ~ 19.3 nm. The somewhat large standard deviation in our nanofiber diameters may arise from the secondary growth, which causes the over-polymerized reaction of nanofibers. So as to comprehend and investigate the intrinsic conduction mechanism in PANI nanofibers, the dedoped, as-synthesized and doped nanofiber thin-film devices are first fabricated for comparisons. The *I-V* curves and temperature dependent

resistance of dedoped, as-synthesized and doped nanofiber thin films are illustrated in Fig. 5.3 (b) and (c), respectively. The *I-V* curves at room temperature for all thin-film devices reveal linear in the measurement range. As seen in Fig. 5.3 (b), PANI nanofiber thin film, doped with HCl acid, responds with a higher resistance decrease of up to ~ 2 orders of magnitude. It has been well-known that the conducting difference in PAIN thin films comes from the degree of protonation [9]. As for the corresponding temperature behaviors, as delineated in Fig. 5.3 (c), in both as-synthesized and dedoped (doped) thin films the resistance as a function of the square root of the inverse temperature appears straight manifestly. The slope of temperature-dependent resistance increases with the increasing of room-temperature resistance of PANI nanofiber thin films. Unlike the inorganic nanostructure such as ZnO nanowires [10] which can be detached from the source sample to disperse onto the substrate, PANI nanofibers cannot be placed arbitrarily on an insulating substrate for elucidating their electrical properties. By utilizing DEP technique, the nanofibers are positioned onto the top of two pre-patterned Ti/Au electrode by electron-beam lithography, as shown in Fig. 5.3 (d). As a result of the shrinking contact area in nanofiber devices, the contact resistance may contribute extremely to the total resistance of two-probe system [11]. Fig. 5.3 (e) depicts the *I-V* curves of a PANI nanofiber device under electron-beam exposure at room temperature. After several times of the electron-beam exposure to the contact area of the PANI nanofiber device, the current increases by at least three orders of magnitude and the nonlinear *I-V* curve gradually is converted to a linear line, indicating an ohmic contact forms and contact resistance can be neglected. The room-temperature resistance of the PANI nanofiber device as a function of electron-beam exposing time is shown in Fig. 5.3 (f). It is emphasized that all of PANI nanofiber devices, discussed in the below paragraphs, are exposed for 1 h.
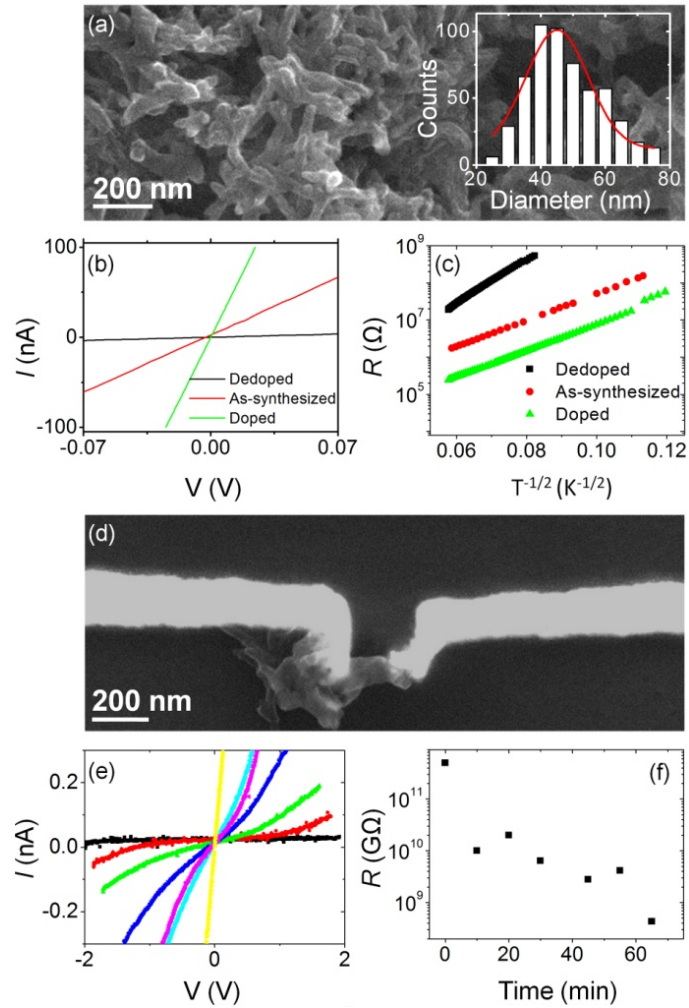
Figure 5.3: (a) FE-SEM image of as-synthesized polyaniline nanofibers with the corresponding size distribution and a red curve fitted according to a Gaussian function, shown in the inset. The average diameter and the standard deviation of nanofibers are evaluated to be about 45.0 and 19.3 nm, respectively. (b) *I-V* behaviors and (c) *R-T* of dedoped, as-synthesized, and doped nanofiber thin films. (d) SEM image of a polyaniline nanofiber device. (e) The change of *I-V* curves of a polyaniline nanofiber device at room temperature after electron-beam exposure. (f) The room-temperature resistance of the nanoscale devices as a function of the electron-beam exposing time.

Resistances as a function of inverse temperature for a series of two-probe PANI nanofiber thin-film devices (L01 and L02) and nanofiber devices (S01-S06), as revealed in Fig. 5.4 (a), have been well-described to follow a hopping transport form for carriers

$$R = R_0 \exp\left(\left(T_0 / T\right)^{1/p}\right) \quad (5.1)$$

, where R and T are resistance and temperature, T_0 is a characteristic temperature, R_0 is a weak temperature-dependent constant, and p is the exponent parameter. The solid lines give the best fitting to data in Fig. 5.4 (a) to derive the exponent parameter, p, shown in the inset. The average value and standard deviation of the exponent parameter p's are 2.08 and 0.275, respectively. The average of T_0 obtained for present nanofiber devices is drawn out to be about 41874 K as well. In addition, it should be noticed that with the variation of the geometric structure from PANI nanofiber thin-film to nanofiber devices, room-temperature resistance increases by 4 orders of magnitude. To our best knowledge, we surmise assertively that the conduction mechanism in PANI nanofibers is ascribed to the Sheng model of charging-energy-limited-tunneling theory (CELT), proposed in 1973 for granular metals in which the conduction is supposed to proceed from tunneling between small conducting grains embedded in a insulting matrix [12]. On the other hand, room-temperature resistance as a function of the ratio of length (L) to cross-sectional area (A) for all PANI nanofiber devices, as displayed in Fig. 5.4 (b), is fitted with the relation of $R \approx \rho L / A$, where ρ is the resistivity of PANI nanofibers. The least-square fitting is performed by a solid line to extract the value of the resistivity $\sim 10^2$ Ω cm.

Before we go ahead to discuss the experimental results in PANI nanofiber devices, we should address more the quantitative validity of our data. Actually, in

additional to the transport theory of CELT, the temperature dependent resistance following a $T^{-1/2}$ law has been widely observed in polymer systems, explained by other theoretical models like Efros-Shklovshii (ES) and one-dimensional (1D) variable range hopping (VRH). In order to examine deliberately our conjecture for the electrical transport of PANI nanofibers, we presume the behavior of temperature dependence of resistance results from ES-VRH theory. According to this model, the localization length of electronic wave function, ξ, could be given by the equation $\xi = 2.8e^2 / 4\pi\varepsilon\varepsilon_0 k_B T_0$ [13], where e, ε, ε_0 and k_B are charge, the permittivity of vacuum, effective dielectric constant of material and the Boltzmann constant, respectively. Using the experimentally obtained T_0 = 41874 K and the typical dielectric constant of conducting polymers, $\varepsilon_0 \sim 2$ [14], the localization length, ξ, is computed to be ~ 0.6 nm. Furthermore, the critical temperature, T_C, can also be evaluated in terms of the mathematical form $T_C = e^4 \xi g_0 / k_B (4\pi\varepsilon\varepsilon_0)^2$ [13], where g_0 is the density of states at Fermi level. Below this critical temperature, the Coulomb interaction cannot be ignored and the temperature dependent resistances comply with ES-VRH theory. Assuming that the density of states of polyaniline, g_0, is about 10^{19} eV^{-1} cm^{-3} [15], the critical temperature, T_C, can be estimated as ~ 35 K in our system which is too low to dominate the transport of electrons in PANI nanofibers so we can exclude this possibility to account for our data. On the other hand, when an applied electric field, E, significantly exceeds a threshold field, E_t, differential resistance (dV / dI) can be expressed as $dV / dI \propto \exp\left(-\left(E_0 / E\right)^{1/d+1}\right)$ [16], where d = 0 and 1 conform to CELT and 1D-VRH model, respectively. E_0 is a constant. Therefore, by analyzing the I-V behaviors at high voltage, we could further distinguish and compare between CELT and 1D-VRH model in our PANI nanofibers, describing in the following paragraph.
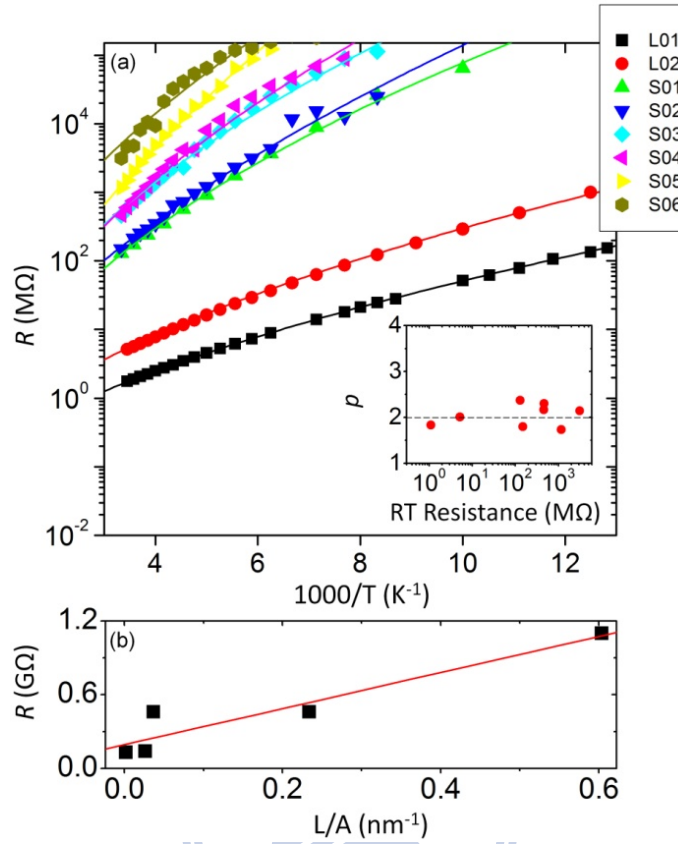
Figure 5.4: (a) Resistance as a function of inverse temperature for two-probe polyaniline nanofiber thin-film devices (L01 and L02) and nanofiber devices (S01-S06). The solid lines represent the best fitting to data in accordance with the charge-energy-limited tunneling theory (*More information is given in Section 2.4*). The fitting exponent, *p*, as function of room-temperature resistance for polyaniline thin-film and nanofiber devices shows in the inset. The average value and standard deviation of the exponent parameter *p*'s are 2.08 and 0.275, respectively. (b) Room-temperature as a function of *L* / *A* for all nanofiber devices. The solid line gives the best linear least square fitting to data.

Fig. 5.5 (a) shows d*V* / d*I* as a function of inverse electrical field (1 / *E*) of S06 nanofiber device at various temperatures. Meanwhile, the same data in the form of

dV / dI versus $E^{-1/2}$ are also plotted in the inset of Fig. 5.5 (a) for comparisons to 1D-VRH model. As can be seen in Fig. 5.5 (a), we observed that all dV / dI curves follow a 1 / E law and collapse clear into a single line in the high-field regime. The dashed line plotted in the Fig. 5.5 (a) indicates the high-field approached curve. In contrast, the data in the plot of dV / dI versus $E^{-1/2}$ in the high-field regime are discrete which demonstrates directly that 1D-VRH is inappropriate for explaining our data. Since we adopted DEP technique to realize nano-approach in PANI nanofiber devices, nanoscale devices can facilitate to explore the behaviors of the mesoscopic charge transport at high electric field. Hence, systematic comparisons and arguments to our data in the low-field regime as well as in the high-field regime, providing enough evidence, help us rule out ES-VRH and 1D-VRH models. Back to the transport model of CELT, the hopping condition in grain systems originates from a basic assumption that $s \times E_C$ should keep a constant everywhere throughout the sample, where s represents the separation distance of the neighboring conducting grains and E_C is the charging energy per grain. The charging energy, E_C, is an energy required to create a positive-negative charged pair to transport an electron between two neutral conducting grains and is inversely proportional to the average diameter of the conducting grains, d (i.e. s / d = constant). In the CELT model, the relationship between s and d can be written as [12]

$$s + d = \left(k_B / 4e\right)\left(T_0 / E_0\right) = \left(k_B / e\right)\left(T / E_t\right) \tag{5.2}$$

$$s / d = \left(k_B T_0 / 16U\right)\left(1 + \sqrt{1 + \left(16U / k_B T_0\right)}\right) \tag{5.3}$$

, where U ~ 2 eV is the Coulomb repulsion energy of two electrons sitting at the distance of monomer size (~ 0.36 nm) of polymers [17]. By using the experimentally obtained T_0 = 55360 K in the low-field regime and E_0 = 1529440 V

/ cm in the high-field regime of S06 nanofiber devices, s and d are calculated to be 3 and 5 nm, respectively, from Eq. (5.2) and (5.3). The estimated value of 8 nm for $s + d$, less than the average diameter of a single PANI nanofiber, appears physically reasonable. Besides, the dotted line in Fig. 5.5 (a) unveils the temperature dependent threshold field, E_t, increasing gradually with the increasing temperature. Furthermore, we can determine the charging energy, E_C, per grain in a single PAIN nanofiber to be about 78 meV by utilizing the formula of

$$E_C = \frac{1}{2} \cdot \frac{e^2}{4\pi\varepsilon\varepsilon_0 d} \cdot \left(\frac{2\,s/d}{1/2 + s/d} \right).$$ This charging energy of 78 meV is significantly large

and supports the feasibleness in observing this hopping conduction of CELT at room temperature. The schematic diagram of the conducting model in the PANI nanofibers is sketched in Fig. 5.5 (b). The solid lines represent individual polyaniline polymer chains. The spheres imply metallic regions of emeraldine salt (ES) form that is surrounded by insulating regions of emeraldine base (EB) form. The average diameter, d, and the separation distance, s, of the conducting region are marked on the graph. Hopping electrons transport between two neighboring metallic regions of emeraldine salt. The behavior of the electron transport in a single PANI nanofiber is attributed to thermally activated tunneling mechanism under low-field condition, and under high-field condition it follows the field-induced tunneling mechanism.
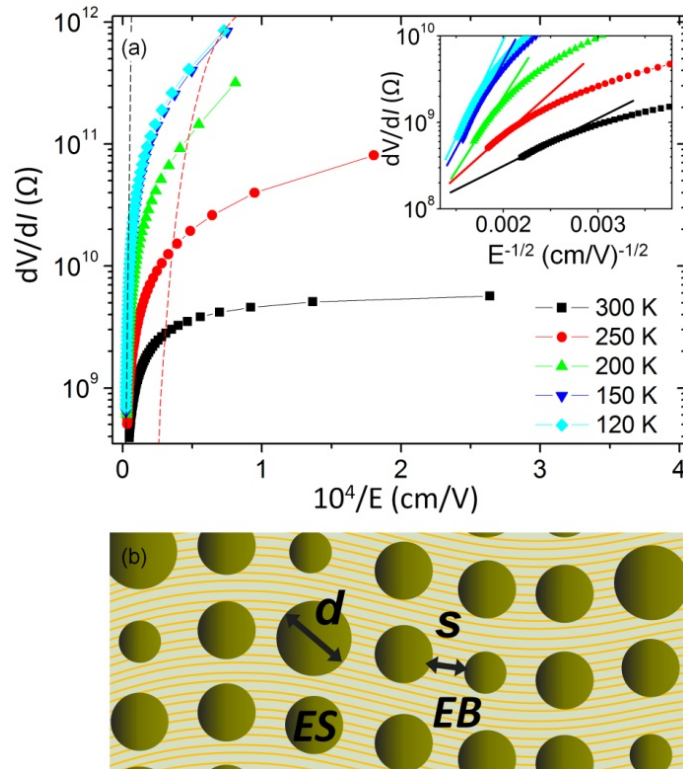
Figure 5.5: (a) d*V* / d*I* vs 1/ *E* curves at different temperatures for S06 device. The dashed and the dotted line represent the limiting behavior at zero temperature and the threshold electrical field at different temperature. The data in the form of d*V* / d*I* vs $E^{-1/2}$ curves also draw in the inset, for comparison. (b) A schematic diagram to model the polyaniline nanofiber. The solid line represents individual polyaniline chains. The spheres imply metallic regions of emeraldine salt (ES) form that is surrounded by insulating regions of emeraldine base (EB) form. The average diameter, *d*, and the separation, *s*, of the conducting region are marked in (b).

References

[1]   X. Lu and Y. Xia, *Nature Nanotech.* 1, 163 (2006)

[2]   S. Hong and S. Myung, *Nature Nanotech.* 2, 207 (2007)

[3]   C. K Chian, C. R. Fincher, Jr. Y. W. Park, A. J. Heeger, H. Shirakawa, E. J. Louis, S. C. Gau and A. G. Macdiarmid, *Phys. Rev. Lett.* 39, 1098 (1977)

[4]   J. Huang, S. Virji, B. H. Weiller and R. B. Kaner, *J. Am. Chem. Soc.* 125, 314 (2003)

[5]   N. J. Pinto, Jt. A. T. Johnson, A. G. Macdiarmid, C. H. Mueller, N. Theofylaktos and F. A. Miranda, *Appl. Phys. Lett.* 83, 4244 (2003)

[6]   R. J. Tseng, J. Huang, J. Ouyang, R. B. Kaner and Y. Yang, *Nano Lett.* 5, 1077 (2005)

[7]   Z. Wei, Z. Zhang and M. Wan, *Langmuir* 18, 917 (2002)

[8]   J. Huang and R. B. Kaner, *Angew. Chem. Int. Ed.* 43, 5817 (2004)

[9]   W. S. Huang, B. D. Humphrey and A. G. MacDiarmid, *J. Chem. Soc., Faraday Trans.* 82, 2385 (1986)

[10] Y. F. Lin, W. B. Jian, C. P. Wang, Y. W. Suen, Z. Y. Wu, F. R. Chen, J. J. Kai and J. J. Lin, *Appl. Phys. Lett.* 90, 223117 (2007)

[11] Y. F. Lin and W. B. Jian, *Nano Lett.* 8, 3146 (2008)

[12] P. Sheng, B. Abeles and Y. Arie, *Phys. Rev. Lett.* 31, 44 (1973) B. Abeles and P. Sheng, M. D. Coutts, *Adv. Phys.* 24, 407 (1975)

[13] B. I. Shklovskii and A. L. Efors, *Electronic Properties of Doped Semiconductro*, New York (1975)

[14] Y. Cao, A. E. Kovalev, R. Xiao, J. Kim, T. S. Mayer and T. E. Mallouk, *Nano Lett.* 8, 4653 (2008)

[15] M. Ghosh, A. Barman, S. K. De and S. Chatterjee, *J. Appl. Phys.* 84, 806 (1998)

[16] Z. H. Wang, E. M. Scherr, A. G. MacDiarmid and A. J. Epstein, *Phys. Rev. B* 45, 4190 (1992)

[17] B. Sixou, N. Mermilliod, J. P. Travers, *Phys. Rev. B* 53, 4509 (1996)

Chapter 6

Conclusion

We have explored the electrical properties in two-probe nanodevices including ZnO, InP, GaP nanowires, and PAIN nanofibers. In two-probe ZnO nanowre devices, we have learned that the nanocontact could give an enormous electrical contact resistance due to the shrinking contact area. According to current-voltage characteristics and temperature dependence of resistances, two-probe nanodevices could be classified into three types, including two Ohmic contacts, one Ohmic and one Schottky contacts, and two back-to-back Schottky contacts. Moreover, the nanocontact can be modeled equivalently as an interfacial disorder electron system and variable range hopping theory of the form $R \propto \exp((T_0 / T)^{1/p})$ is used to describe the electrical transport. The exponential parameter, *p*, rises from 2 to 4 with an increase of specific contact resistivity, indicating a change from one- to three-dimensional hopping. To analyze in many two-probe nanodevices of different system of semiconductor nanowires, an unambiguous universal trend of a rising exponent parameter with an increasing specific contact resistivity has been detected.

Utilizing two-probe electrical measurement strategy, the contact- or NW-dominated devices are separated each other. The determination of intrinsic

electrical properties of ZnO, InP and GaP nanowires has been demonstrated. In the case that a nanocontact resistance is superior or comparable to a nanowire resistance, low resistance at room temperature implies an electron transport nature in nanowires. In contrast, effects of the nanocontact can be neglected if the nanowire resistance is considerably high. Using this two-probe technique, the electron transport of intrinsic ZnO and InP nanowires at high temperatures obeys thermally activated transport and it follows three-dimensional Mott variable range hopping at low temperatures. Due to relative high intrinsic resistance in GaP nanowires, the electron behaviors can be explained by using thermally activated transport. Based on this two-probe measurement, the carrier concentration at room temperature in ZnO, InP and GaP nanowires have also been drawn out to be 10^{19}, 6×10^{15}, and 1.5×10^{14} cm^{-3}, respectively. Furthermore, both nanowire- and contact-dominated InP nanowire devices were exposed to light and oxygen gas to see any different responses. Surprisingly, in comparison with the nanowire-dominated devices, the contact-dominated devices always exhibit a much higher ratio of resistance changes in response to either light or oxygen gas exposures. Hence, the contact-dominated devices might be applied to a good photo- or gas-sensor, rather than the NW-dominated devices in the future.

On the other hand, by utilizing dielectrophoresis technique polyaniline nanofibers are moved and positioned onto two nanoscale electrodes with a nanogap of 150-300 nm between them successfully. This nanotechnological approach is applied to measurements of electric field dependence of differential resistance of polyaniline nanofibers under a high electric field while in a low voltage. Systematically comparisons and discussions offer sufficient evident to exclude other theoretical models like Efros-Shklovskii and one-dimensional Mott variable range hopping. Through fitting to charge-energy-limited-tunneling theory, the size

71

of conductive grain, the separation distance between two grains, and the charging energy per grain in a single polyaniline nanofiber are estimated to be about 5 nm, 3 nm, and 78 meV.

Curriculum Vitae

Personal Data:

Name: Yen-Fu Lin   Birthday: Dec. 3, 1981

Nationality: Taiwan (R.O.C.)   Birthplace: Taichung County

Sex: Male

E-mail: yanfu.ep94g@nctu.edu.tw

Education:

2005 ~ 2010   Ph.D. in Dep. of Electrophysics, National Chiao Tung University, Hsinchu, Taiwan.

2001 ~ 2005   B.S. in Dep.of Physics, Tunghai Hai University, Taichung, Taiwan.

1998 ~ 2001   National Chung Hsing Senior High School, Nantou, Taiwan.

Work Experience:

2007~2008   T. A. of Applied Maths. II - Differential Equation

2008~2009   T. A. of Applied Maths. II - Differential Equation

Specialty:

Nano Devices

Low Temperament Physics Experiments

Solid State Physics Experiments